

DEM PARAMETER CALIBRATION METHODOLOGY FOR COHESIVE POWDERS USING A RING SHEAR TESTER

by

Prathamesh Nilesh Sankhe

A Thesis

Submitted to the Faculty of Purdue University

In Partial Fulfillment of the Requirements for the degree of

Master of Science in Mechanical Engineering



School of Mechanical Engineering

West Lafayette, Indiana

August 2021

THE PURDUE UNIVERSITY GRADUATE SCHOOL
STATEMENT OF COMMITTEE APPROVAL

Dr. Carl Wassgren, Chair

School of Mechanical Engineering

Dr. Stephen Beaudoin

School of Chemical Engineering

Dr. Marcial Gonzalez

School of Mechanical Engineering

Approved by:

Dr. Nicole L. Key

Dedicated to my parents for their unwavering love and belief.

ACKNOWLEDGMENTS

I would like to thank my advisor, Prof. Carl Wassgren, for giving me the opportunity to work on this project sponsored by AbbVie. This work would not have been possible without his continued support and guidance throughout the project. I appreciate the multiple opportunities he provided me to show initiative and showcase the research more effectively. I want to express my gratitude to Prof. Gonzalez and Prof. Beaudoin for their guidance and for serving on my examining committee. I would like to also thank the School of Mechanical Engineering for giving me the opportunity to work as a TA for a semester. The experience helped me refine my knowledge and communication skills. I appreciate all the help the wonderful people from the ME Graduate Office provided me with that helped me through any issues I faced through the two years of graduate school.

I would also like to thank the wonderful team I worked with at AbbVie on this project. Dr. Ketterhagen, Dr. Vogt, and Dr. Capece were there with aid whenever I needed help. I appreciate the help I got from my research colleagues at CP3 especially from Zhengpu, Cara, Nathan, and Abhishek. I am also thankful to all the fantastic professors I had throughout all the courses I took at Purdue.

I was lucky enough to have an amazing group of peers and friends supporting me throughout my time at Purdue. Among others, I would like to thank Varshi, Akash, Aryamaan, and Kaan for always being there for me and help create wonderful memories in the six years at Purdue. I would like to thank Varshi again for being there for me throughout the COVID-19 pandemic and helping me get through graduate school.

Finally, I would also like to thank my parents for their continuous and unconditional encouragement and love, and for always being there for me even while being thousands of kilometers away. They have done everything in their power to help me succeed and help me achieve my dreams and goals.

TABLE OF CONTENTS

LIST OF TABLES	6
LIST OF FIGURES	7
NOMENCLATURE	10
ABSTRACT.....	12
1. INTRODUCTION	13
2. BACKGROUND	15
2.1 Experimental bulk calibration measurements	15
2.2 Literature summary	20
3. OBJECTIVES	25
4. DEM MODELING	26
4.1 DEM Contact Models	26
4.2 Shear Cell Discrete Element Model and Setup	29
4.3 Flodex Discrete Element Model and Setup	32
5. DIMENSIONAL ANALYSIS AND DESIGN OF EXPERIMENTS	35
5.1 Dimensional Analysis	35
5.2 Parameter Selection and Design of Experiments	38
6. CALIBRATION METHODOLOGY AND VALIDATION RESULTS	43
6.1 Predictive Models	43
6.1.1 Incipient Internal Friction Angle	45
6.1.2 Critical State Internal Friction Angle	48
6.1.3 Dimensionless Bulk Cohesion	50
6.2 Parameter Correlation	53
6.3 Model Optimization	55
6.4 Modification for HPMC: Addition of particle shape factor.....	59
6.5 Validation using Flodex Tester	63
7. SUMMARY AND CONCLUSIONS	71
8. RECOMMENDATION FOR FUTURE WORK	75
REFERENCES	79

LIST OF TABLES

Table 5.1: List of independent input parameters in a DEM shear cell simulation.....	36
Table 5.2: List of dimensionless parameters in a DEM shear cell simulation.....	37
Table 5.3: Baseline DEM simulation parameter values.....	39
Table 5.4: Dimensionless DEM input parameters used in the design of experiments	40
Table 6.1: Summary of experimental density measurements for lactose, HPMC, ABT-089.....	57
Table 6.2: Summary of experimental shear cell measurements at different end consolidation stresses for lactose, HPMC, ABT-089.....	57
Table 6.3: Summary of calibration and partial validation error results	58
Table 6.4: Updated calibration and partial validation error results for HPMC with an increased aspect ratio ($Ar=2$)	61
Table 6.5: Summary of calibrated parameter values for all three powder samples at different end consolidation stresses.....	62
Table 6.6: Summary of Flodex experimental measurements and simulation results	64
Table 6.7: Summary of results for the Flodex factory sensitivity study	66

LIST OF FIGURES

Figure 2.1: Schematic showing first few steps of an incipient yield measurement (left) and the incipient yield locus generated using the values (right).....	16
Figure 2.2: Plot comparing the measured incipient yield locus compared to the linear approximation used for calculation for a lactose powder sample at 2000 Pa.....	17
Figure 2.3: Plot showing the yield locus with the Mohr's circles for the unconfined yield strength, f_c , and the consolidating stress, σ_1 represented (Schulze, 2008).....	17
Figure 2.4: Schulze ring shear cell tester RST-XS (left) and Hanson Research's Flodex tester (right) (Hanson Research Corporation 2004).....	18
Figure 2.5: Representation of a DEM particle (circle with a dashed outline) modeling a collection of real particles (solid grey circles).....	19
Figure 4.1: Hertz-Mindlin model compared to the JKR theoretical model and its EDEM implementation (DEM Solutions, 2014).....	27
Figure 4.2: Schematic of the 3-D computational domain that models an annular shear cell as a parallel plate simulation.....	30
Figure 4.3: EDEM simulation of a shear cell with parallel plates and the periodic boundaries along with the computational domain boundaries highlighted in red.....	30
Figure 4.4: 2-D representation of the shear cell procedure used in the simulation	31
Figure 4.5: 2-D representation of the Flodex operating procedure used in the DEM simulations.....	33
Figure 4.6: Schematic of the 3-D computational domain that models the Flodex tester in DEM	34
Figure 5.1: Diagram showing significance of using design of experiments to run full factorial studies over varying one factor at a time	38
Figure 5.2: Shear cell data output and processing from DEM simulations – (a) Raw top plate shear stress data outputted from the ring shear cell DEM simulations, (b) Window average of raw data across 100 data points (1 second simulation time), and range for the steady state value calculation	42
Figure 6.1: Example of a box plot with all appropriate data points represented	44
Figure 6.2: Interaction effects for combination of parameters in pairs on the bulk cohesion response of a simulated annular shear cell, where, σ_{end} refers to σ_{end} , PSD refers to σ_{dd} , Y_{pp} refers to γ_{pp} and u_{pp} refers to μ_{pp}	45
Figure 6.3: Main effects of each design of experiments parameter on the incipient internal friction angle, the values corresponding to very low, low, and high for each parameter can be found in Table 5.4	47

Figure 6.4: Pareto chart showing standardized effects for all terms for incipient internal friction angle response of a simulated annular shear cell.	48
Figure 6.5: Main effects of each design of experiments parameter on the critical state internal friction angle, the values corresponding to very low, low, and high for each parameter can be found in Table 5.4	49
Figure 6.6: Pareto chart showing standardized effects for all terms for critical state internal friction angle response of a simulated annular shear cell	50
Figure 6.7: Main effects of each design of experiments parameter on the dimensionless bulk cohesion, the values corresponding to very low, low, and high for each parameter can be found in Table 5.4	51
Figure 6.8: Pareto chart showing standardized effects for all terms for dimensionless bulk cohesion response of a simulated annular shear cell.....	52
Figure 6.9: Correlation between incipient internal friction angle and dimensionless bulk cohesion	54
Figure 6.10: Correlation between incipient internal friction angle and critical internal friction angle	54
Figure 6.11: Surface plot representing the fitting of the predictive model from equation 6.3 with the dimensionless bulk cohesion simulation data at 2kPa represented as blue dots	55
Figure 6.12: HPMC particle morphology showing fibrous particles captured by HPMC characterization work done by Allenspach et al., (2020).....	60
Figure 6.13: Capsule-shaped particle modeled in DEM using five particles in a glued-sphere model (an individual particle part of the glued-sphere highlighted in red)	60
Figure 6.14: Change in the calibrated $\gamma E'd$ value with a change in the end consolidation stress for all three powder samples (lactose, HPMC, ABT-089)	62
Figure 6.15: Flodex DEM simulation (without cohesion) slice showing mechanical arching for larger particle diameter for particle diameter to orifice diameter ratio of 12	64
Figure 6.16: HPMC DEM simulation slice showing the particle fill (left) and one of the final successful passes (right) for particles with non-spherical shapes	65
Figure 6.17: The three separate factory cases tested in the factory radius and height sensitivity analysis.....	66
Figure 6.18: Flodex DEM simulation showing larger mound formation for ABT-089 for smaller factory diameters.....	67
Figure 6.19: Flodex DEM simulation showing the resulting failure due to the high mound formation causing extensive arches for ABT-089 at a disk diameter of 32mm	68
Figure 6.20: Flodex DEM simulation slice showing clogging of factories for lower factory sizes with the particle factory highlighted in cyan at the top	69

Figure 8.1: Schematic of the linear Hysteretic Spring contact model force-displacement relationship showing different loading and unloading curves with the red arrows showing the loading directions..... 77

NOMENCLATURE

f_c	Unconfined yield strength
σ_1	Consolidating stress
ϕ_{crit}	Shear cell critical state internal friction angle
σ_{end}	Shear cell end consolidation stress
ϕ_{inc}	Shear cell incipient yield internal friction angle
c	Bulk cohesion
τ	Shear stress
σ	Normal stress
F_n	Normal contact force
γ	Cohesive surface energy density
δ_n	Normal overlap
E'	Effective elastic modulus
R^*	Equivalent radius
ν	Poisson's ratio
δ_c	JKR model normal overlap threshold
F_n^d	Normal damping force
v_n^{rel}	Normal component of the relative velocity
m^*	Equivalent mass
S_n	Normal stiffness
ε	Coefficient of restitution
δ_t	Tangential overlap
S_t	Tangential stiffness
G^*	Equivalent shear modulus
F_t^d	Tangential damping force
μ_R	Coefficient of rolling friction
$\hat{\omega}_{rel}$	Relative rotational velocity unit vector
\bar{d}	Mean particle diameter
ρ	Particle density

σ_d	Particle diameter standard deviation
v_{wall}	Shear cell bottom wall velocity
ψ_{max}	Angle of max dilation
A_r	Particle aspect ratio

ABSTRACT

Discrete element method (DEM) modeling is a common way to model particulate systems and processes. Since the number of particles in most pharmaceutical processes is incredibly large, modeling these substantial magnitudes of particles individually using DEM is not computationally reasonable. To simplify the DEM modeling, agglomerates or groups of particles are modeled instead. This change creates a disconnect between the real particle parameter values and the simulated particle parameter values. Thus, efficient and accurate calibration is needed for effective modeling.

The methodology proposed in this thesis utilized a single commonly used bulk flowability measurement device, an annular shear cell, to calibrate for these DEM parameters with the help of dimensional analysis, design of experiments, and statistical tools. Three bulk responses were studied from the ring shear cell: the incipient yield internal friction angle, the critical state internal friction angle, and the bulk cohesion. The most important DEM parameters were isolated and subjected to a dimensional analysis to increase the generality of the results. A modified full-factorial study was then set up using the identified dimensionless parameters. The final calibration results were then validated using an independent flow through an orifice test using a FlodexTM.

This thesis demonstrates this proposed calibration methodology using three different powder samples, lactose, (hydroxypropyl) methyl cellulose (HPMC), and ABT-089. Using the DEM simulation results and the experimental measurements, predictive models were created for all three powder samples. For HPMC, the calibration errors were large while using spherical particles, so a non-spherical particle shape was introduced using the glued-sphere model in DEM. The calibration process was repeated with simulated non-spherical particles with an aspect ratio of two to create a new model for HPMC.

The overall calibration procedure and the three models, when validated with the Flodex simulations and measurements, successfully predicted the Flodex results within one Flowability index range for all three powder samples. This demonstrates that this methodology can be used to successfully calibrate various DEM simulation parameters.

1. INTRODUCTION

Particles in all forms play an important role in a variety of industries dealing with materials ranging from pharmaceutical powders to food grains to geotechnical samples. The discrete element method (DEM) is an increasingly important tool for studying these particulate systems. With innovations in computing hardware, DEM simulations are more extensively used in different industries to model particle interactions and granular flow. DEM is notably used in the fields of chemical engineering, agriculture, pharmaceuticals, and metallurgy.

Initially developed by Cundall and Strack, (1979) DEM models two particles as rigid bodies, and interaction forces are calculated based on the overlap between the particles. This soft-sphere model has been since then iterated upon by numerous researchers (e.g., Di Renzo and Di Maio, 2004; Vu-Quoc and Zhang, 1999). However, quantitatively accurate values and qualitatively meaningful trends are contingent on the accuracy of the contact model along with the values of particle property parameters chosen as input to the simulation (Benvenuti et al., 2016). The choice of these input parameters is a key limitation for the effective application of DEM (Wilkinson et al., 2017). The values of these parameters used in the simulations need to be reasonable for the accurate modeling of systems.

These particle level DEM parameters are difficult to measure. Obtaining a measured value for input parameters on a particle level is extremely time consuming and requires extensive measurement techniques for a comprehensive dataset. Recently, there has been work in accurately determining particle properties like the elastic modulus on a particle level (Leisen et al., 2012; Marigo et al., 2014). Due to computational limitations, the scale of DEM simulations is limited in terms of particle size and number. Frequently, particle size is artificially increased to decrease the computational load while maintaining the accuracy of results (Obermayr et al., 2014; Ucgul et al., 2014). Thus, using individual particle parameters will still lead to a mismatch since the typical particle sizes used in DEM simulations are larger than real life particle sizes. This mismatch is also the case with modeling complex particle shapes. Complex particles can be modeled as an individual sphere with an additional parameter of rolling resistance (Ketterhagen et al., 2007) or a multi-sphere model (Lu and McDowell, 2007) in DEM to reduce the computational load.

Since particle level DEM parameters are difficult to measure, bulk scale calibration is relied on to obtain DEM input parameters. Some common bulk tests used for this purpose are shear

cell tests, angle of repose tests, and the FT4 rheometer measurements. These bulk test input values will usually not result in the same output value as that of particle level parameters and thus calibration is done to scale the values to the correct level. Ideally, these bulk scale tests should be simple to perform experimentally and computationally, and they should depend on a single DEM parameter so that the parameter can be calibrated with confidence. Multi-parameter dependent calibration tests can cause interactive effects between the parameters being ignored and thus leading to a sub-optimal calibration.

This thesis investigates the incipient and critical state bulk response of a shear cell simulated using DEM. Shear cells are commonly used as part of DEM calibration, but to date, there have been no published studies that comprehensively look at a wide parameter space and interactive dependence while using dimensional analysis. The purpose of this work is to investigate a wide range of parameters to determine their effects on the bulk level response of a shear cell. Using the design of experiments to reduce the number of simulations needed and to measure interactive effects and comparing the simulation results with experimental measurements, a calibrated model to predict powder behavior is created. To validate the calibrated model, the parameter values are used to model flow through an orifice using the Flodex.

2. BACKGROUND

2.1 Experimental bulk calibration measurements

Annular shear cells have been used for flowability measurements and bulk calibration previously in multiple studies (Angus et al., 2020; Karkala et al., 2019; Simons et al., 2015). A shear cell is generally used to measure a powder's yield strength as a function of the consolidation stress (Schwedes and Schulze, 1990). The measurements made using the shear cell enable the calculations for the unconfined yield strength, f_c , consolidating stress, σ_1 and can help determine the material's flow function.

Shear cells do not directly measure the two stresses, the unconfined yield strength, f_c , consolidating stress, σ_1 , but use Mohr's circle analysis to get the stress values. In addition to the two stresses, they can also be used to measure a material's internal friction angle and bulk cohesion. A common shear cell used for these measurements is the Schulze ring shear cell tester RST-XS. A shear cell can operate in two ways: a critical state measurement and an incipient yield measurement. A critical state measurement involves measuring the shear stress a particle bed requires to continue flow at no volume change for a certain normal consolidation stress. It is an individual point instead of a locus and can be the first point in the incipient yield locus at that normal stress and solid fraction.

$$\tau = \tan(\phi_{crit}) \cdot \sigma \quad Eq. 2.1$$

$$\tau = \tan(\phi_{inc}) \cdot \sigma + c \quad Eq. 2.2$$

The relationship between the normal stress and shear stress is given by Eq. 2.1 and can be numerically given by the critical state internal friction angle, ϕ_{crit} . The incipient yield measurement involves multiple measurement points for a particle bed at a certain fixed solid fraction but at different stresses. The measurements create a locus that represents the shear stress required to initiate powder flow at that solid fraction and consolidation stress. The solid fraction is maintained between measurements by using a fixed end consolidation stress, σ_{end} . The procedure begins with this initial stress and then each measurement after is done at lower normal stresses to create a locus by plotting the normal stress and the max shear stress at each normal stress. This procedure is better represented in Figure 2.1 via steps.

The ideal Mohr-coulomb material results in a linear fit to this yield locus as given by Eq. 2.2. Real materials show significant curvatures at lower normal stresses in the incipient yield locus, but the approximation can be used to compute the incipient internal friction angle, ϕ_{inc} , and bulk cohesion, c , for real materials as well. An experimental measurement with curvature compared with the linear approximation for a lactose powder sample at 2kPa end consolidation stress is shown in Figure 2.2. The yield locus can be used to find the two aforementioned stresses, the unconfined yield strength, f_c , and the consolidating stress, σ_1 , using the Mohr's circles and yield locus. This relationship is shown in Figure 2.3 with the two Mohr's circles with a visual illustration of what both the stresses represent (Schulze, 2008).

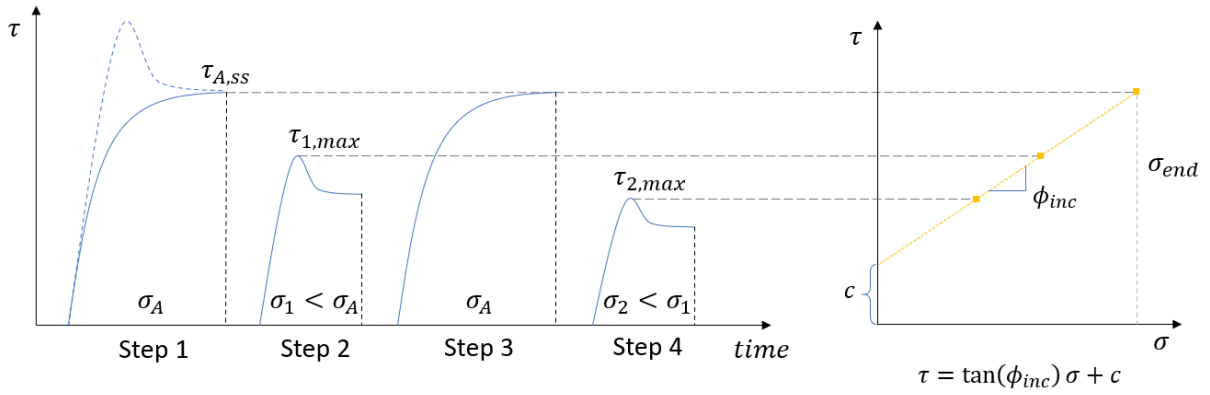


Figure 2.1: Schematic showing first few steps of an incipient yield measurement (left) and the incipient yield locus generated using the values (right)

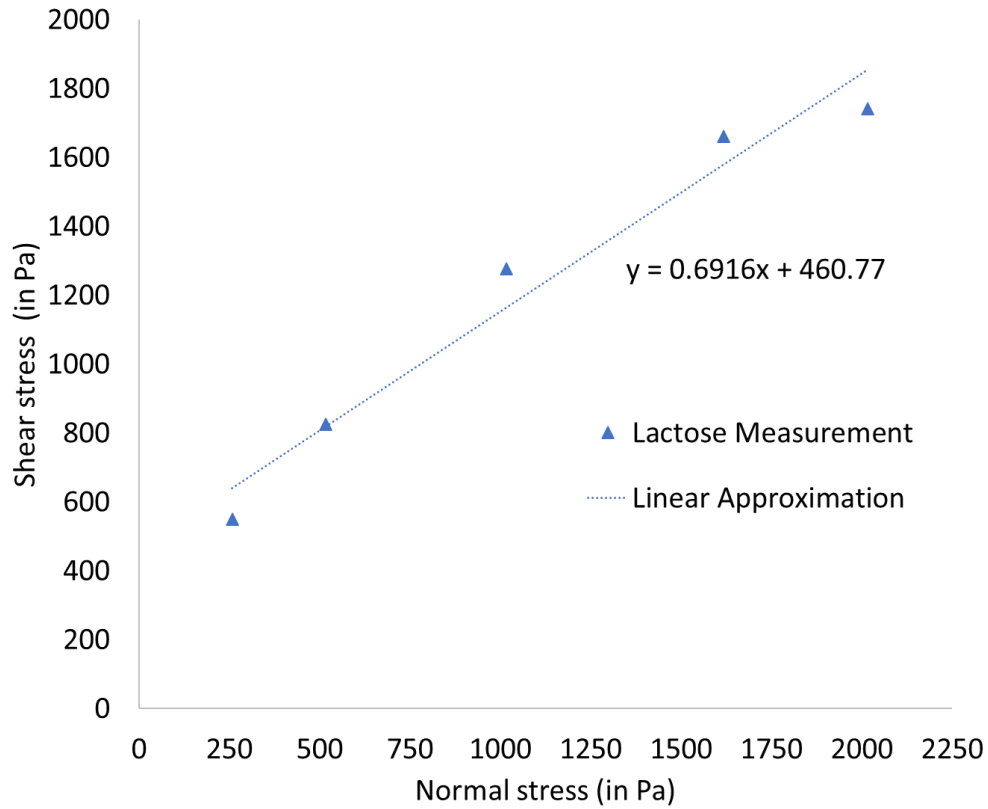


Figure 2.2: Plot comparing the measured incipient yield locus compared to the linear approximation used for calculation for a lactose powder sample at 2000 Pa

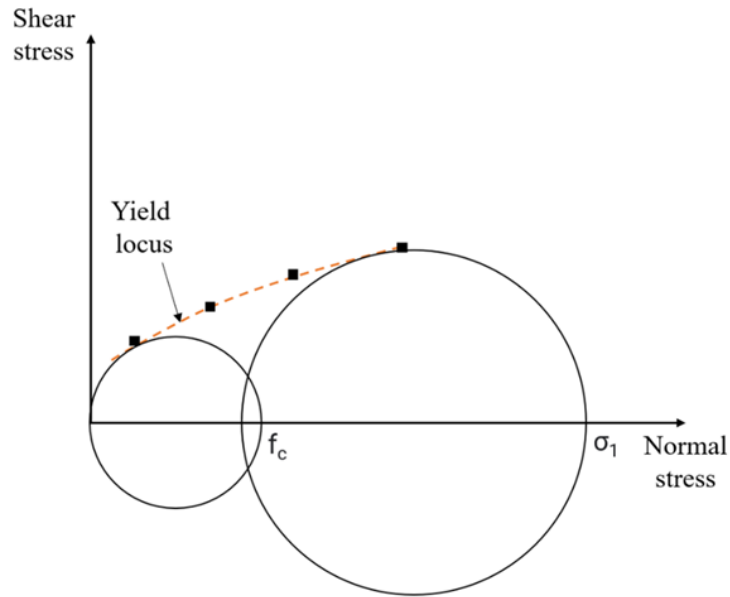


Figure 2.3: Plot showing the yield locus with the Mohr's circles for the unconfined yield strength, f_c , and the consolidating stress, σ_1 represented (Schulze, 2008)

The flowability of material used in tablet formulation is of paramount importance in tablet production. The term powder flowability is used to represent the ability of the powder to flow evenly in a variety of processes like feed flow through a hopper, compaction, or fluidization. Numerous parameters determine powder flowability some of which include particle size, particle density, powder bulk density, particle shape, porosity, and powder cohesion. Additionally, this measurement is often closely related to the measurement technique used. Since there is variability based on the measurement technique used, it is often used as a comparative measure to compare flow behavior between different materials. The flowability index can also be used in correlations, for example in Schiano et al., (2018), the flowability index measured was used to correlate with the critical filling speed in an experimental study with pharmaceutical powders for a rotary die filling system.

The powder flowability can be measured using a flow through an orifice as discussed in USP chapter <1174> Powder Flow (USP, 2016). A common way of testing this flowability measure is by using the Flodex™ tester. The flowability is quantified by the smallest diameter through which the powder flows through in three consecutive attempts. A flowing powder could become non-flowing when forced through small openings leading to jams (Lavoie et al., 2002). The two flowability measurement devices, the Schulze shear cell tester RST-XS, and the Flodex tester are shown in Figure 2.4.



Figure 2.4: Schulze ring shear cell tester RST-XS (left) and Hanson Research's Flodex tester (right) (Hanson Research Corporation 2004)

The flow characteristics of a material can also be determined using the poured bulk density and the tapped bulk density of the material in the form of a Hausner ratio. Hausner ratio is the ratio of the tapped bulk density and the poured bulk density as given by Equation 2.3. Poured bulk density is measured using the mass of a powder sample and the volume of the sample after it is first poured into a cylinder. Tapped bulk density is measured using the same mass of a powder sample but the volume of the sample is measured after the cylinder containing the sample has been tapped in a standard manner as prescribed in the USP chapter <1174> Powder Flow (USP, 2016).

$$\text{Hausner ratio} = \frac{\rho_{\text{tapped}}}{\rho_{\text{poured}}} \quad \text{Eq. 2.3}$$

The Hausner ratio test can be used as a calibration or a validation test for DEM simulations. But after an initial set of Hausner ratio simulations, it was observed that the powder column did not densify as much after tapping as compared to the experimental measurement. This difference was attributed to the DEM particles being larger than the real particles. In the DEM simulations, each DEM particle is approximately modeling a collection of real interior particles as shown in Figure 2.5. As the particle column is tapped, the real materials fill the voids in an experiment, and the particle column densifies leading to a higher solid fraction. But the same is not the case with the DEM simulations as the DEM particle has a predetermined solid fraction that does not change over simulation time. So even if the larger DEM particles can move around and fill larger voids, the smaller interior particles that these large DEM particles are representing cannot move or densify the column further. This leads to incorrect modeling of the process. This can be avoided by varying the particle size during the simulation to accurately model this densification. As a result of this limitation in modeling the Hausner ratio experiment, it was not used any further in this work for calibration or validation.

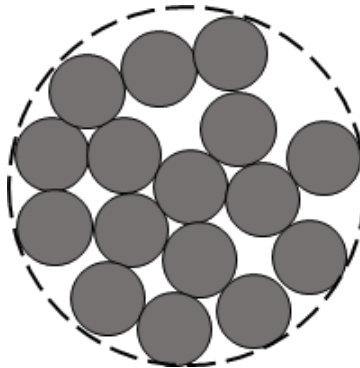


Figure 2.5: Representation of a DEM particle (circle with a dashed outline) modeling a collection of real particles (solid grey circles)

2.2 Literature summary

The literature has established that DEM has been successfully used to model a diverse set of particle handling processes like the flow from a hopper (Anand et al., 2008; Ketterhagen et al., 2009), bulk compression (Hassanpour and Ghadiri, 2004; Martin and Bouvard, 2003), powder mixing (Alizadeh et al., 2014; Marigo et al., 2011), screw conveyors (Owen and Cleary, 2009; Shimizu and Cundall, 2001), and die filling (Guo et al., 2011; Wu, 2008). But the accurate and efficient modeling of processes is dependent on reliable calibration.

The typical parameters to be calibrated include the coefficient of sliding friction between materials, cohesion interaction parameters between materials, coefficient of restitution, the elastic modulus, Poisson's ratio, coefficient of rolling resistance, and particle size distribution parameters. Particle shape also plays a critical role in DEM modeling and typically particles are modeled as spheres with a rolling resistance to consider any irregular shape effects that cause rolling resistance. If a non-spherical particle has to be modeled, it is frequently modeled using the glued-sphere approach (Favier et al., 1999) by modeling a non-spherical particle as a cluster of multiple spheres. Some common bulk calibration tests include static angle of repose test, dynamic angle of repose test, the ring shear cell test, uniaxial compression test, and FT4 rheometer test. These parameters can also be directly measured on a particle level using a particle level measurement, but particle level measurements might not directly translate to a good model as DEM particles tend to be larger than real particles.

Coetzee, (2017) reviewed multiple different calibration practices for DEM parameters in his work. The work covers both a particle level measuring approach and a bulk calibration approach. It was concluded that a direct particle level measurement technique is ideal but hard to realize with smaller particles. Several properties can be measured using this approach like particle density, Young's modulus, sliding friction coefficients, and coefficient of restitution. Values measured using a direct measurement approach are independent of the contact model used, however, they are difficult to measure and cannot be used directly when particles are scaled up for modeling. The results obtained using this approach frequently had to resort to using the bulk calibration approach to obtain more accurate results. As mentioned in the previous section, Coetzee's work also concluded that if particle sizes are scaled up due to computational limitations, this approach would not result in accurate bulk behavior. Further, it was noted that the bulk calibration approach was more popular because of the simple application of the tests used.

However, the experiments might have to be repeated numerically for more accurate calibration. Another major limitation of this bulk calibration method is the dependence of the parameter values on the contact model used.

Ranjan, (2017) presented a calibration methodology for DEM parameters. The work first identified the most important DEM input parameters required for successful modeling. Next, appropriate calibration tests were designed for these identified parameters. Finally, the parameter calibration results were validated by comparing a simulation and the experimental measurement of a dynamic test in a rheometer using three different materials: glass beads, Ottawa sand, and mustard seeds. The key DEM parameters identified were the coefficient of sliding friction, coefficient of rolling friction, coefficient of restitution, particle stiffness, moduli of elasticity and shear, and Poisson's ratio. All these parameters were calibrated or measured using different sets of measurements. For the coefficient of sliding friction and rolling friction, two bulk tests in the form of an angle of repose test and a shear cell test were used. The results from both tests were combined to get a better calibration for the parameters. A uniaxial compression test was used for the Young's modulus and a vibrated bed test was used to calibrate for the coefficient of restitution. Finally, the calibrated values of the parameters were validated using a FT4 rheometer simulation and experimental measurement where the torque due to the blades of the mixer was monitored and compared. A key limitation was that particle size was not varied and no cohesion parameters were calibrated.

Another calibration approach that used artificial neural networks was carried out by Benvenuti et al., (2016). In this study, a feed forward artificial neural network was trained using a bulk calibration experiment and DEM simulation data for the shear cell test. This was used to get an estimate of the sensitivity of the output to the parameters chosen. Next, this artificial neural network and sensitivity results were used to predict the macroscopic ensemble behavior in relation to different sets of bulk calibration tests. The trained artificial neural network was utilized to forecast the output of a larger set of bulk calibration simulations compared to the initial set of input parameters. This led to a predicted set of parameters that could accurately predict the particle properties of the material used. It was found that the new set of parameters was smaller than the initial set of combinations thus optimizing the solution map to a narrower region. For each calibration test, the network needs to be trained once. Thus, multiple bulk calibration tests and

their respective artificial neural networks can be used to accurately narrow the solution down to a single set of input parameters.

Wilkinson et al., (2017) made use of the design of experiments technique to reduce the complexity and number of simulations involved in a parameter dependence study of a Freeman rheometer. They performed a full factorial analysis for five particle properties: Young's modulus, sliding friction coefficient, rolling friction coefficient, coefficient of restitution, and cohesion energy density using three sets of values (low, baseline, and high). The study showed that full factorial design transitioning to a reduced factorial design can be used to accurately predict key parameters from a bulk calibration test. Finally, it was concluded that the FT4 Rheometer can be used to calibrate the particle sliding friction coefficients and rolling friction coefficients as DEM input parameters for powders. Statistical design of experiments (DoE) has been also used to provide a more efficient approach to investigating roller compaction (Souihi et al., 2013). Similar techniques were used by Yoon, (2007) and Hanley et al., (2011) for reduction of the number of simulations and exploring wider parameter spaces.

Simons et al., (2015) performed a sensitivity analysis of individual parameters on an agitated mixer by coupling it with a ring shear cell for a mixture of cohesive particles. They varied a set of parameters independently to conduct a sensitivity analysis on each. The study concluded that Young's modulus, particle-particle sliding friction, and particle-particle rolling friction individually influence the bulk response of the shear cell. It should be noted that this sensitivity analysis was done for cohesive particles while varying one parameter at a time and thus any interactive effects were ignored. Further, the particle size and distribution were not varied in this study.

Work by Ketterhagen, (2018) looked at a periodic section of an annular ring shear tester and FT4 rheometer to simulate the effects of various particle properties on the bulk flow behavior. This analysis was conducted to simulate the behavior of a wide array of parameters for typical pharmaceutical powders. Thousands of cloud-based DEM simulations were conducted to develop an extensive simulation dataset that can provide a starting point to a potential DEM calibration project using a lookup table. The parameters that varied were the friction coefficients, coefficients of restitution, and the surface energy for particle-particle and particle-geometry interactions. The study concluded that the coefficients of restitution did not affect the bulk response of either the shear cell or the FT4 rheometer. It was concluded that as a set, the two bulk calibration tests were

dependent on the particle-particle sliding friction the most followed by the cohesion/adhesion surface energy density for both contacts and the particle-geometry sliding friction.

There have been more investigations into wider DEM parameter spaces for other processes. Asaf et al., (2007) investigated the discrete element parameter space for soil tillage. They concluded that the determination of two primary model parameters, sliding friction, and spring constant, was sufficient to model the soil-tool interaction. Kretz et al., (2016) investigated a screw feeder system using DEM simulations using durum wheat semolina as the material using the Blender software. The model was created by setting a fitting criteria between the simulations and the experiments for an angle of repose, and measurements of shear force constant and wall friction using a Jenike shear cell. After validating the model using mass flow rate measurements, it was concluded that these parameters were adequate to model the process effectively.

The scaling of DEM particle parameters is critical in reducing computational time. Work done by Hærvig et al., (2017) on reduced particle stiffness DEM simulations focuses on guidelines for these computational time reductions. They note that this is necessary because the models in DEM combined with high particle stiffness result in time steps in the order of nanoseconds, which makes this DEM impractical for use. To ensure reasonable timesteps, they scale the Young's modulus down significantly. However, this affects the implementation of the cohesion model used, the Johnson-Kendall-Roberts (JKR) model in this work, and thus they end up scaling the cohesion surface energy density to accommodate for these particles with lower stiffness. This secondary scaling is to ensure that even with reduced stiffness the border between sticking and rebounding behavior is intact.

A major problem with modeling particles with irregular shapes in DEM is the cohesion models used and the parameter values associated with them. Multiple models have been used to model cohesion across various works to model this cohesive behavior. But since these model parameters are calibrated using bulk calibration approaches and particle sizes are usually scaled up, these models are very specific to the application they are calibrated for. Some common models used to model cohesion in granular flow are the Johnson-Kendall-Roberts (JKR) model used in studies by Behjani et al., (2017); X. Chen and Elliott, (2020); and Loreti and Wu, (2018), parallel bond contact model (PBCM) used in studies by Chen et al., (2013), Sadek et al., (2011), and R. Zhang and Li, (2006), and elasto-plastic adhesive contact models used in studies by Yuan Guo et al., (2021), Kamrin, (2010), and Vu-Quoc and Zhang, (1999).

The literature shows a variety of approaches have been adopted for bulk calibration for accurate use of DEM to model powder particle behavior. A common bulk calibration test used is the shear cell test. But most studies have focused on individual parameter dependence and past studies have not investigated a wider look into the complete experimental space of parameters for the shear cell. Furthermore, interactive dependence on parameters for the bulk response of a shear cell using parametric studies or design of experiments analysis has not been considered and neither has the use of dimensional analysis to improve adaptability. This investigation of the effect of single or multiple parameter dependence of the bulk response of a shear cell using DEM is a good foundation for the path to efficient and fast calibration.

3. OBJECTIVES

The goal of this thesis is to utilize a widely used bulk flow testing device, an annular shear cell, to calibrate for selective DEM parameters and generate a model in order to predict cohesive powder flow behavior with efficiency and accuracy. The predictive model will assist in pharmaceutical process design and development. To help achieve this, the objectives of this thesis work are:

- 1) Isolate a wide range of parameters that affect the bulk incipient yield and critical state response of a shear cell
- 2) Perform a design of experiment analysis using a factorial study on these isolated parameters and simulate the bulk behavior using DEM
- 3) Understand the impact of these DEM input parameters on the incipient internal friction angle, critical state internal friction angle, and dimensionless bulk cohesion
- 4) Develop a model by calibrating the DEM simulations with the experimental measurements and validate the model using an independent study

4. DEM MODELING

The commercial Discrete Element Method solver, EDEM ©, and EDEMPy © were used for modeling, simulating, and post-processing the simulation results and calculations. The proceeding sub-sections describe the DEM contact models, simulation setups, and procedures used to analyze the shear cell and the Flodex tester.

4.1 DEM Contact Models

The contact model used in EDEM to compute the normal force component is based on Hertzian contact theory. The tangential force is computed based on the work of Mindlin-Deresiewicz (Mindlin and Deresiewicz, 1953). The normal and tangential forces both have damping components with the damping coefficient dependent on the coefficient of restitution (Tsuji et al., 1993). The cohesion model is based on the JKR contact theory developed by Johnson, Kendall, and Roberts, (1971). In addition to the normal force in the Hertzian contact theory, there is an additional cohesion force involved as well.

The normal force is calculated as a function of normal overlap δ_n and the cohesion surface energy density, γ , with the dimensions of energy per unit area, between the two materials as:

$$F_n = -4\sqrt{\pi\gamma E'} a^{\frac{3}{2}} + \frac{4E'}{3R^*} a^3 \quad Eq. 4.1$$

And the normal overlap can be given as:

$$\delta_n = \frac{a^2}{R^*} - \sqrt{\frac{4\pi\gamma a}{E'}} \quad Eq. 4.2$$

where E' is the equivalent elastic modulus and R^* is the equivalent radius as defined as:

$$\frac{1}{E'} = \frac{(1 - \nu_i^2)}{E_i} + \frac{(1 - \nu_j^2)}{E_j} \quad Eq. 4.3$$

$$\frac{1}{R^*} = \frac{1}{R_i} + \frac{1}{R_j} \quad Eq. 4.4$$

with E_i, ν_i, R_i and E_j, ν_j, R_j being the elastic modulus, Poisson's ratio, and radius of the spheres in contact. The Hertz-Mindlin contact model compared to the JKR model and its EDEM implementation is shown in detail as a plot in Figure 4.1. The negative term in the equation just

represents the cohesive force between the two materials. The two models have a slight offset due to the extra term in the JKR model and the JKR model extends beyond the range of the Hertz-Mindlin model. For the case where $\gamma = 0$, the JKR model normal force turns into the Hertz-Mindlin normal force. For the EDEM implementation, there is a maximum gap between particles for a non-zero force as shown in Figure 4.1 by δ_c , the overlap threshold below which the model returns zero force discontinuously (DEM Solutions, 2014).

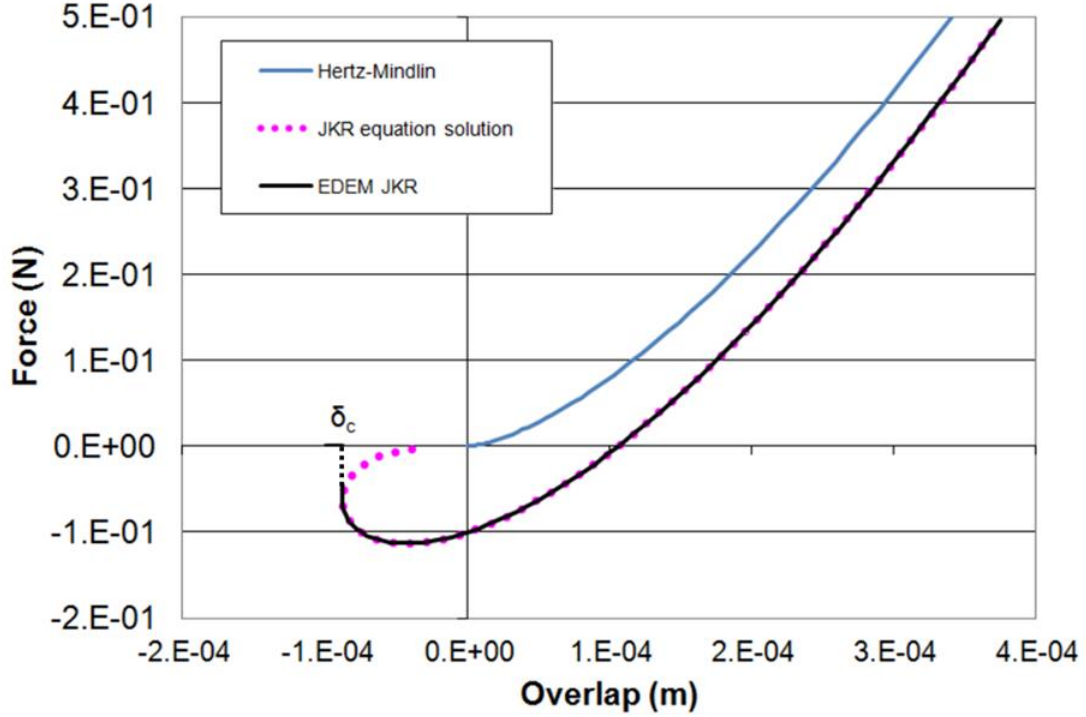


Figure 4.1: Hertz-Mindlin model compared to the JKR theoretical model and its EDEM implementation (DEM Solutions, 2014)

Additionally, there is a normal damping force F_n^d , which is given by

$$F_n^d = -2 * \sqrt{\frac{5}{6}} \beta \sqrt{S_n m^*} v_n^{rel} \quad Eq. 4.5$$

where v_n^{rel} is the normal component of the relative velocity and the equivalent mass (m^*), β , and the normal stiffness (S_n) are given by:

$$\frac{1}{m^*} = \frac{1}{m_1} + \frac{1}{m_2} \quad Eq. 4.6$$

$$\beta = \frac{-\ln \varepsilon}{\sqrt{\ln^2 \varepsilon + \pi^2}} \quad \text{Eq. 4.7}$$

$$S_n = 2E' \sqrt{R^* \delta_n} \quad \text{Eq. 4.8}$$

with ε being the coefficient of restitution.

The tangential friction follows the Coulomb law of friction model (Cundall and Strack, 1979) and is dependent on the tangential overlap (δ_t) and the tangential stiffness (S_t) as follows:

$$F_t = -S_t \delta_t \quad \text{Eq. 4.9}$$

with

$$S_t = 8G^* \sqrt{R^* \delta_n} \quad \text{Eq. 4.10}$$

where G^* is the equivalent shear modulus. Additionally, the tangential damping is given by:

$$F_t^d = -\min \left(u_s |F_n|, 2 * \sqrt{\frac{5}{6}} \beta \sqrt{S_t m^*} v_t^{rel} \right) \quad \text{Eq. 4.11}$$

where v_t^{rel} is the tangential component of the relative velocity.

In addition to the tangential force, a particle rolling resistance is also often included and is modeled as a torque (Zhou et al., 2002):

$$M = -\mu_R |F_N| R^* \hat{\omega}_{rel} \quad \text{Eq. 4.12}$$

where μ_R is coefficient of rolling resistance, $\hat{\omega}_{rel}$ is the unit vector of relative rotational velocity and R^* is the equivalent radius of the two elements in contact.

This rolling resistance torque is added to the torque due to the tangential force to account for resistance to rolling due to particle surface irregularities. Since real particles are not true spheres like they are modeled in DEM, there are surface imperfections that act to resist the rolling of the particles. To account for this behavior in DEM simulations, the rolling resistance is added as an additional torque. This model has been successfully used in several previous DEM studies to model hopper flow (Ketterhagen et al., 2009), flow down an incline (Zhang et al., 2004), and angle of repose experiments (Zhou et al., 2002). Rolling resistance is included to accurately model the non-spherical shapes of most granular material. The present work is completed with particle rotation completely eliminated to replicate the rotational dynamics of non-spherical particles in dense granular flows. In this case, the contact models mentioned previously are the same. However, the coefficient of rolling resistance and the moment of inertia for each particle are set to large numbers and therefore the tangential forces do not affect the rotation of the particles.

4.2 Shear Cell Discrete Element Model and Setup

The discrete element method is used to model the shearing of a granular bed of material in an annular shear cell. The system consists of cohesive, frictional spheres with varying diameters d and a specified density ρ . The sphere diameters are selected from a Gaussian distribution with a small, fixed standard deviation σ_d .

The computational domain is a section of a 3D annular shear cell tester with the horizontal sides modeled as two parallel plates with vertical sides modeled as periodic boundary conditions. Gravity is included in the DEM simulations. Similar to the Schulze ring shear tester, the top, and the bottom plates are modeled as planar surfaces with fins protruding out to prevent particles from sliding directly along the plates. Due to extensive computational demands for modeling a full annular shear cell, rectangular periodic boundary conditions were implemented in the horizontal direction. The use of periodic boundary conditions decreases the computational time and computational power required significantly and only a part of the shear cell tester needs to be simulated to predict the behavior of the whole system. The usage of periodic boundary conditions allows us to model the particle without any effect from the shear cell inner and outer wall. Further, it allows the particles the two translational degrees of freedom in the horizontal direction.

The geometry is defined by the following dimensions: the top plate width (w), the top plate length (l), plate separation distance (H), fin width (w_{fin}), fin length (l_{fin}), and fin separation distance (d_{fin}). The fin separation distance is chosen such that when one fin exits the periodic boundary, another enters on the other end of the periodic boundary. The number of particles in the domain is determined by a specified initial plate separation distance. This specified plate separation distance changes during the simulation. The values for the remaining parameters are based on the Schulze shear cell tester used for experimental measurements. The geometry is shown in Figure 4.2 and an EDEM simulation state modeling the shear cell is shown in Figure 4.3. Since the bottom plate is the only geometry that moves within the domain of the simulation and to accommodate for the periodic boundaries, it is modeled as one long piece with repeated fins at constant intervals that extend beyond the domain of the simulation. The length of the bottom plate is determined based on the total time of the simulation while the width is the same as that of the top plate. The top plate is just modeled as an individual geometry since it does not move in the DEM simulation.

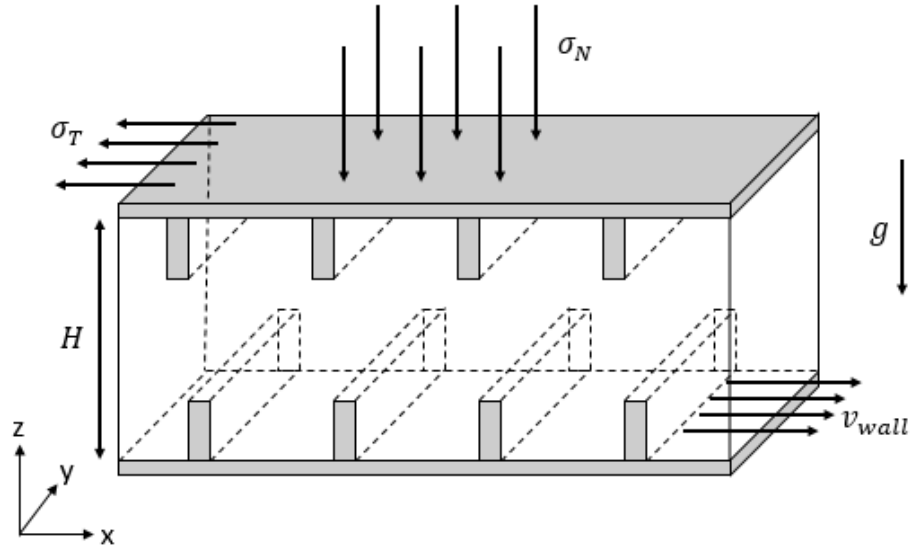


Figure 4.2: Schematic of the 3-D computational domain that models an annular shear cell as a parallel plate simulation

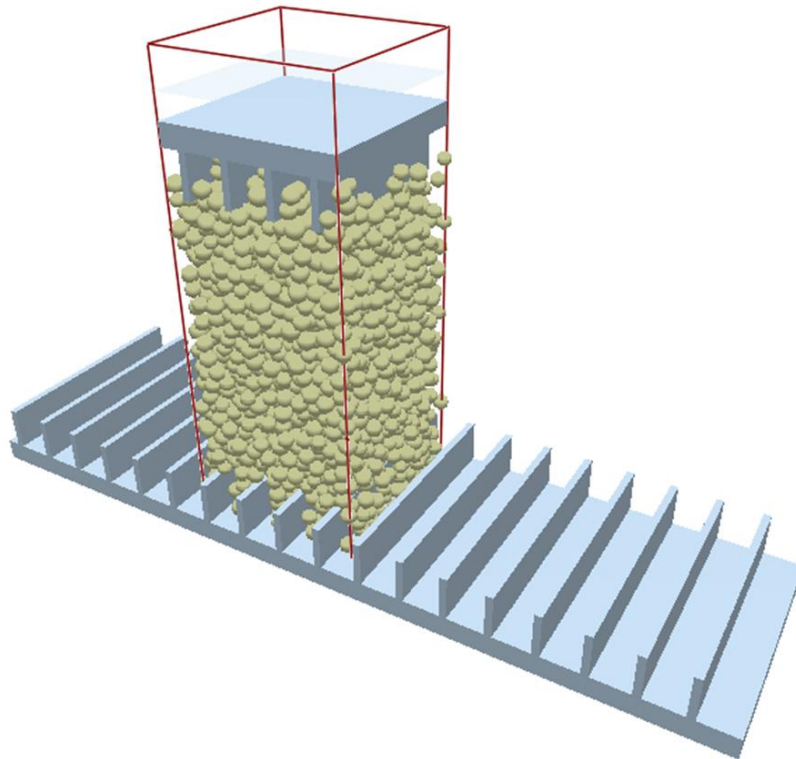


Figure 4.3: EDM simulation of a shear cell with parallel plates and the periodic boundaries along with the computational domain boundaries highlighted in red

The general computational procedure for a set of shear cell simulations is as outlined as follows in Figure 4.4. First, a particle column is generated by assigning each particle a random position and until the specified plate, separation height matches the particle column height. The particles are allowed to settle under gravity on top of the bottom plate until the total kinetic energy decreases below a threshold through inelastic, frictional contacts. Now, the top plate comes down with a specified end consolidation normal stress σ_{end} onto the particle column. After some time, the bottom plate is displaced by a specified velocity v_{wall} . During the shearing process, the variable values relevant to the parameters of interest, the tangential stress σ_T , are recorded at predefined time steps. Finally, the simulation concludes when the total specified simulation time is reached, or steady state is reached, whichever one occurs first. This process is repeated for the incipient yield measurements at normal stress values lower than σ_{end} with reconsolidation between two separate values. Since DEM simulation states can be exported, the simulation state at the conclusion of the initial simulation with the consolidation stress equal to the σ_{end} value can be exported. This state can be reused as a starting point for all the lower normal stress values in the incipient yield locus simulations without the need to rerun the initial simulation. This approach also enables the user to run multiple simulations in parallel once the initial σ_{end} simulation has finished running.

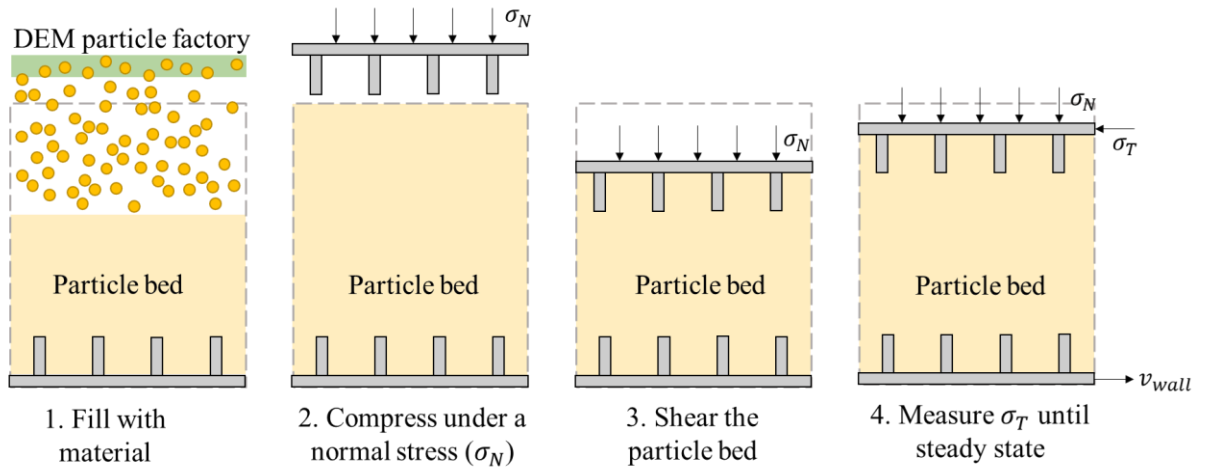


Figure 4.4: 2-D representation of the shear cell procedure used in the simulation

4.3 Flodex Discrete Element Model and Setup

The discrete element method is used to model the flow through an orifice experiment using the FlodexTM tester. The particles used in this setup were similar to the particles used in the shear cell experiment with a specified size distribution and density.

The Flodex tester consists of a cylinder with an open top and replaceable disks with orifices of varying diameters at the bottom. (Geiger et al., 2007; Kumar et al., 2013). In this study, the calibrated parameters were tested on a flow through an orifice experiment using a Flodex tester. The geometry for the DEM simulations was replicated using the device measurements. The procedure used was referenced and given in the Flodex Operation Manual procedure (Hanson Research Corporation, 2004). The bottom orifice can be closed using a stopper connected to the assembly which can be released when needed using a lever. The cylinder was loaded using a funnel setup 2 cm above the cylinder. After the material added had settled for a minute, the bottom stopping plate was released using the release lever on the device. The test was considered a success if the hole at the bottom was visible from the top of the cylinder. The Flowability Index is the diameter of the smallest opening in mm through which the powder flows through successfully on three consecutive attempts. The test was started with the 16-mm disk and depending on the success or failure of the 16-mm disk, the diameter of the disk was decreased or increased repeatedly until the outcome changed.

The Flodex DEM model was created to replicate the experiment so that there were no discrepancies in the measurements and simulations. The Flodex geometry was replicated in a CAD file with the same dimensions as the original Flodex. The loading funnel was replicated using a factory at the top opening of the Flodex. The operating procedure was identical to the one laid out by Hanson Research Corporation, (2004) and is described in detail in Figure 4.5. The material was loaded into the Flodex cylinder using an EDEM factory with random particle position generation within the factory and zero velocity. The material was allowed to settle for an adequate amount of time, 30 seconds in the experiment and 1 second in the simulation. The bottom orifice was opened later. The test was deemed a success if there was a clear pass of material in the center and failure if not. A clear pass of material was defined as being able to see the bottom orifice clearly when looking through the top of the Flodex cylinder. Unlike the shear cell, since each Flodex simulation run is dependent on a completely new particle fill, each Flodex run must start anew without using previous end states.

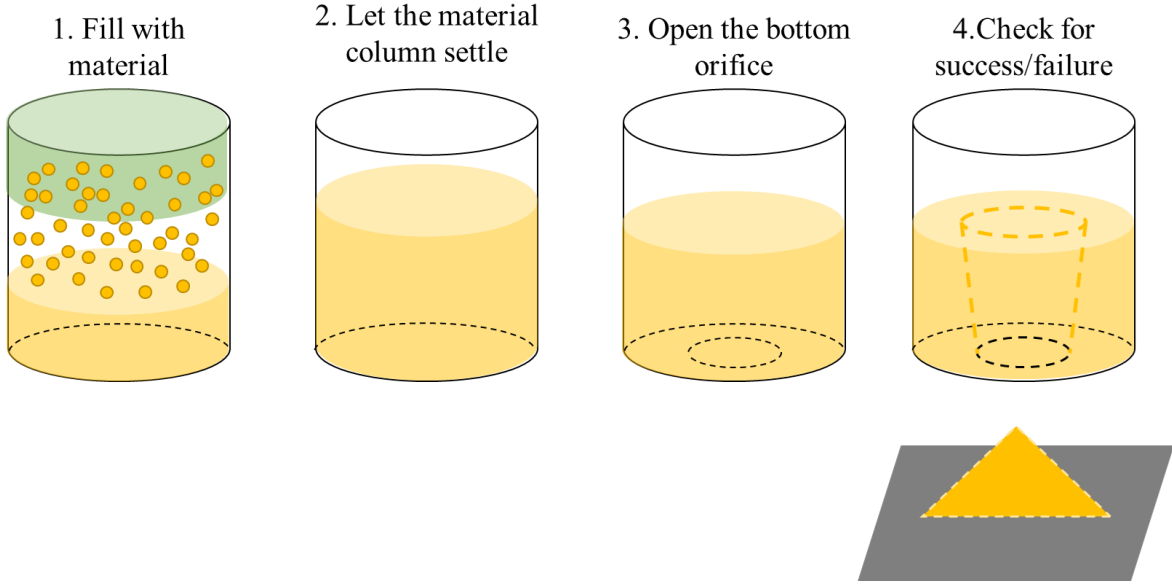


Figure 4.5: 2-D representation of the Flodex operating procedure used in the DEM simulations

The geometry is defined by the following dimensions: the Flodex height (H_{Flodex}), the Flodex diameter (d_{Flodex}), the Flodex factory height from the top of the Flodex ($H_{Flodex\ factory}$), the Flodex factory diameter ($d_{Flodex\ factory}$), and the orifice diameter ($d_{Flodex\ bottom\ orifice}$). The number of particles in the domain is determined by the height of the Flodex, the Flodex is filled until around two-thirds of the Flodex is filled. The geometry is shown in Figure 4.6. The values for the real Flodex device measurements were used for the Flodex height (H_{Flodex}) and the Flodex diameter (d_{Flodex}) values. The orifice diameter ($d_{Flodex\ bottom\ orifice}$) was changed based on the case being tested. The values for the Flodex factory height from the top of the Flodex ($H_{Flodex\ factory}$) and the Flodex factory diameter ($d_{Flodex\ factory}$) were chosen to model the filling conditions in the experimental setup.

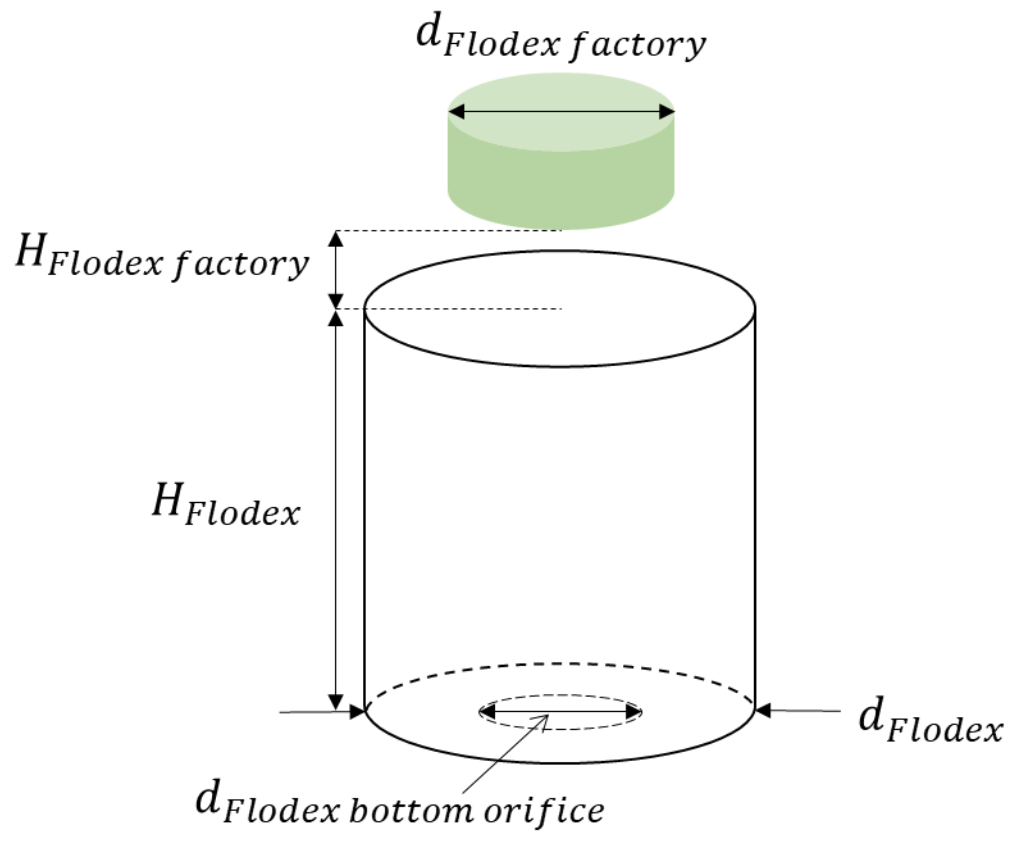


Figure 4.6: Schematic of the 3-D computational domain that models the Flodex tester in DEM

5. DIMENSIONAL ANALYSIS AND DESIGN OF EXPERIMENTS

5.1 Dimensional Analysis

The hypothesis of a dimensional analysis is that the value of the dependent variable in a well-defined process will be the same if all the quantities that define that process are known and have the same values. For example, if the quantity of interest is X_o and it is a dependent variable in the process, we can find the number of dimensionless parameters that X_o depends on using dimensional analysis. These dimensionless parameters can be then found using combined information from experiments, experience, and analysis. In the present work dimensional analysis is performed to simplify the study and determine the relevant parameters to check dependence on. Before conducting the dimensional analysis, the following assumptions were made:

1. The particle size distribution can be expressed by two parameters, e.g., a normal distribution.
2. All of the particles are solid spheres.
3. Wall parameters have no influence on the shear strength of the particle bed.
4. The shear cell dimensions are sufficiently large so that they have no influence on the shear strength of the particle bed.
5. The flow behavior is a function of the effective elastic modulus (defined in Equation 4.3) rather than the elastic modulus and Poisson's ratio independently.

The first step in the dimensional analysis is to isolate a complete set of independent variables in the system that the parameters of interest could depend on. Based on the assumptions made, the three key bulk parameters measured in a shear cell in both the incipient yield mode and critical state mode which are the incipient internal friction angle (ϕ_{inc}), the critical state internal friction angle (ϕ_{crit}), and the bulk cohesion (c) are expected to be a function of independent parameters listed in Table 5.1.

Table 5.1: List of independent input parameters in a DEM shear cell simulation.

#	Parameter	Symbol	Dimensions
1	mean particle size	\bar{d}	L
2	size distribution standard deviation	σ_d	L
3	particle density	ρ	M/L ³
4	effective elastic modulus (from Eq. 4.3)	E^*	F/L ² = M/(LT ²)
5	particle-particle sliding friction coefficient	μ_{pp}	-
6	particle-particle coefficient of restitution	ε_{pp}	-
7	cohesive surface energy density	γ_{pp}	E/L ² = M/T ²
8	applied normal stress	σ_{end}	F/L ² = M/(LT ²)
9	wall speed	V	L/T

Again, the effective elastic modulus (E^*) incorporates both Young's modulus (E) and Poisson's ratio (ν) and is given by the following:

$$E^* = \left[\frac{(1 - \nu^2)}{E} \right]^{-1} \quad Eq. 5.1$$

Following this, a set of reference dimensions is set for the dependent variable, in the case of a purely mechanical problem, all quantity dimensions can be defined as a factor of length, mass, and time. Next, the Buckingham-Pi Theorem is used to identify the number of dimensionless parameters. The Buckingham-Pi theorem defines that the total number of dimensionless parameters, also known as Π -terms, is given by the difference between the number of parameters and the reference dimensions. The present work has 9 independent parameters as mentioned in Table 5.1 and 3 reference dimensions. Thus, the Buckingham-Pi theorem gives us the following number of dimensionless parameters.

$$(\# \Pi \text{ terms}) = (\# \text{independent variables}) - (\# \text{ref. dimensions}) = 9 - 3 = 6 \quad Eq. 5.2$$

The dimensionless parameters formed using the set of independent parameters outlined in Table 5.1 are given below in Table 5.2:

Table 5.2: List of dimensionless parameters in a DEM shear cell simulation.

#	Parameter	Symbol
1	relative standard deviation of PSD	σ_d/\bar{d}
2	eff. elastic modulus to applied stress ratio	σ_{end}/E'
3	eff. elastic modulus to dynamic pressure	$E'/(\rho V^2)$
4	particle-particle sliding friction coefficient	μ_{pp}
5	particle-particle coefficient of restitution	ε_{pp}
6	ratio of cohesive-to-elastic force	$\gamma_{pp}/(E'\bar{d})$

This study can be further simplified by eliminating parameters without significant impact on the parameters of interest. It is reasonable to assume that at sufficiently slow wall speeds, the coefficient of restitution and effective elastic modulus to dynamic pressure ratio effects can be ignored. This assumption is supported by results from previous analysis by Ketterhagen, (2018). Further, to maintain dimensional integrity, the bulk cohesion (c) is also represented as a dimensionless ratio, $\left(\frac{c}{E'}\right)$, between the bulk cohesion and the effective elastic modulus (E').

Hence, as a result of the dimensional analysis, the incipient internal friction angle, the critical state internal friction angle, and the dimensionless bulk cohesion are expected to be functions of the following Π terms,

$$(\phi_{incp}) = f \left[\frac{\sigma_d}{\bar{d}}, \frac{\sigma_{end}}{E'}, \mu_{pp}, \frac{\gamma_{pp}}{E'\bar{d}} \right] \quad Eq. 5.3$$

$$(\phi_{crit}) = g \left[\frac{\sigma_d}{\bar{d}}, \frac{\sigma_{end}}{E'}, \mu_{pp}, \frac{\gamma_{pp}}{E'\bar{d}} \right] \quad Eq. 5.4$$

$$\frac{c}{E'} = h \left[\frac{\sigma_d}{\bar{d}}, \frac{\sigma_{end}}{E'}, \mu_{pp}, \frac{\gamma_{pp}}{E'\bar{d}} \right] \quad Eq. 5.5$$

where f , g , and h are unknown functions.

These three bulk responses, ϕ_{incp} , ϕ_{crit} , and $\frac{c}{E'}$, are functions of the dimensionless parameters, $\frac{\sigma_d}{\bar{d}}$, $\frac{\sigma_{end}}{E'}$, μ_{pp} , and $\frac{\gamma_{pp}}{E'\bar{d}}$. Thus, the values of individual parameters can be changed while keeping the dimensionless parameter value constant and as a result not changing the value of the bulk response. For example, if the value of \bar{d} is halved, the bulk response values can be kept constant by halving σ_d and γ_{pp} , since the values of $\frac{\sigma_d}{\bar{d}}$ and $\frac{\gamma_{pp}}{E'\bar{d}}$ stay constant. This is a useful benefit

of dimensional analysis when it comes to DEM simulations as individual input variable values often have to be changed to reduce computational load. This can be done without any issues by using dimensional analysis.

5.2 Parameter Selection and Design of Experiments

Traditionally, experiments and simulations are carried out using a linear approach where one parameter is varied at a time while keeping the rest constant. The effect of the parameter varied on the output is then measured. This approach leads to an incomplete mapping of the sensitivity of the output variable as only the corners of the parameter space are captured in this method. In this approach, the interactive effects of various parameters are completely ignored while only exploiting a limited small part of the experimental space. The true relationship between the multiple variables and the experimental output cannot be completely explained with this analysis if there are any potential interactive effects, thus resulting in a sub-optimal solution. This difference in the two methods of experimental analysis, varying one factor at a time vs factorial analysis, is shown visually in Figure 5.1. The highlighted regions and the parameter value sets show the additional range of experimental space explored with just 4 additional sets of experiments using factorial analysis.

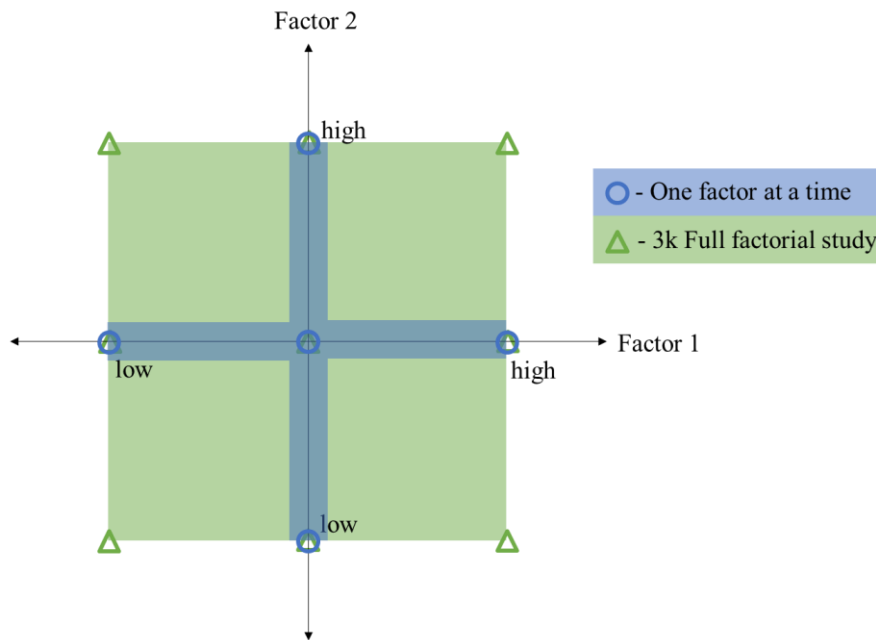


Figure 5.1: Diagram showing significance of using design of experiments to run full factorial studies over varying one factor at a time

The design of experiments approach covers the complete experimental space while reducing the amount of computation required. Further, interactive effects between two or more factors can be explored with the same, resulting in a more directional approach towards an optimal solution. Along with that, a design of experiments approach leads to a robust database of experimental values for multivariate analysis. A similar approach is used in this study to accurately predict the individual and interactive dependence of the experimental output, bulk friction coefficient, and solid fraction, on the variables isolated using the dimensional analysis. The design of experiments dataset is an excellent starting point for checking further dependence of individual parameters. The independent parameters were given baseline values as shown in Table 5.3.

Table 5.3: Baseline DEM simulation parameter values.

#	Parameter	Symbol	Baseline Value
1	mean particle diameter	\bar{d}	2 mm
2	particle size distribution standard deviation	σ_d	0.2 mm
3	particle density	ρ	1000 kg/m ³
4	effective elastic modulus	E'	10 MPa
5	particle-particle sliding friction coefficient	μ_{pp}	0.40
6	particle-particle coefficient of restitution	ε_{pp}	0.9
7	cohesive surface energy density	γ_{pp}	0.1 J/m ²
8	applied normal stress	σ_{end}	2 kPa
9	wall speed	v_{wall}	3 mm/s

The particle parameter, mean particle diameter, particle density, effective particle elastic modulus, particle-particle sliding friction coefficient, particle-particle coefficient of restitution, cohesive surface energy density, baseline values were selected using literature and previous DEM work. The particle diameter standard deviation is chosen at 10% of the mean diameter. The wall speed was selected to be 3 mm/s based on past work on DEM modeling of a shear cell using parallel plates (Ketterhagen et al., 2009). The applied normal stress is a typical value used in annular shear cell experiments.

To conduct a full-factorial study on the four dimensionless parameters to a level of 2, a total of 16 simulations are required. Thus, an array of values covering the entire experimental space was created by varying the parameter values from the baseline value based on a design of experiments variation. This initial design of experiments array was modified by extending the range of values for σ_{end} and γ_{pp} by one additional low value to investigate low consolidation loads and low cohesion, respectively after the initial set of results. The modified 2k full factorial study would thus require 36 simulations in total, including the 16 mentioned previously. The resulting values to be varied for the design of experiments array are as given in Table 5.4.

Table 5.4: Dimensionless DEM input parameters used in the design of experiments

#	Parameter	Symbol	Values
1	relative standard deviation of PSD (normal distribution)	σ_d/\bar{d}	0.07, 0.13
2	applied end point normal stress to effective elastic modulus	$\frac{\sigma_{end}}{E'}$	0.70e-4, 3.47e-4, 6.94e-4 (for $\sigma_{end} = 0.4 \text{ kPa}, 2\text{kPa}, 4\text{kPa}$)
3	ratio of cohesive-to-elastic force	$\frac{\gamma_{pp}}{E'\bar{d}}$	8.68e-7, 4.34e-6, 4.34e-5 (for $\gamma_{pp} = 0.01, 0.05, 0.50 \text{ J/m}^2$)
4	particle-particle sliding friction coefficient	μ_{pp}	0.3, 0.5

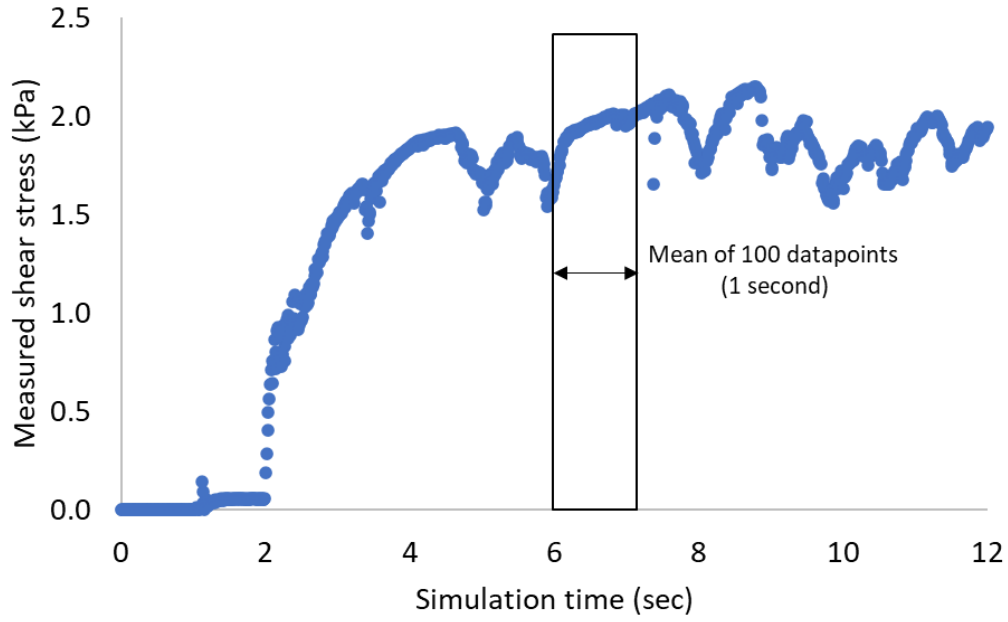
For each set of parameter values in Table 5.4, a shear cell simulation was run to get the incipient and critical state bulk response. A full-factorial analysis was conducted on the results of these simulations to find the parameters that had a statistically significant effect on the bulk output, which is discussed further in the following section.

The shear cell simulations once finished were post-processed. The shear stress and normal stress values on the top plate and on the particle bed were exported to a datasheet for processing. After exporting the values, the data is checked for noise as DEM simulations tend to have noise and constant fluctuations in their exported data. To avoid this issue of noise in the data and have smoother processing, this stress data is taken through a window mean to reduce the noise. A

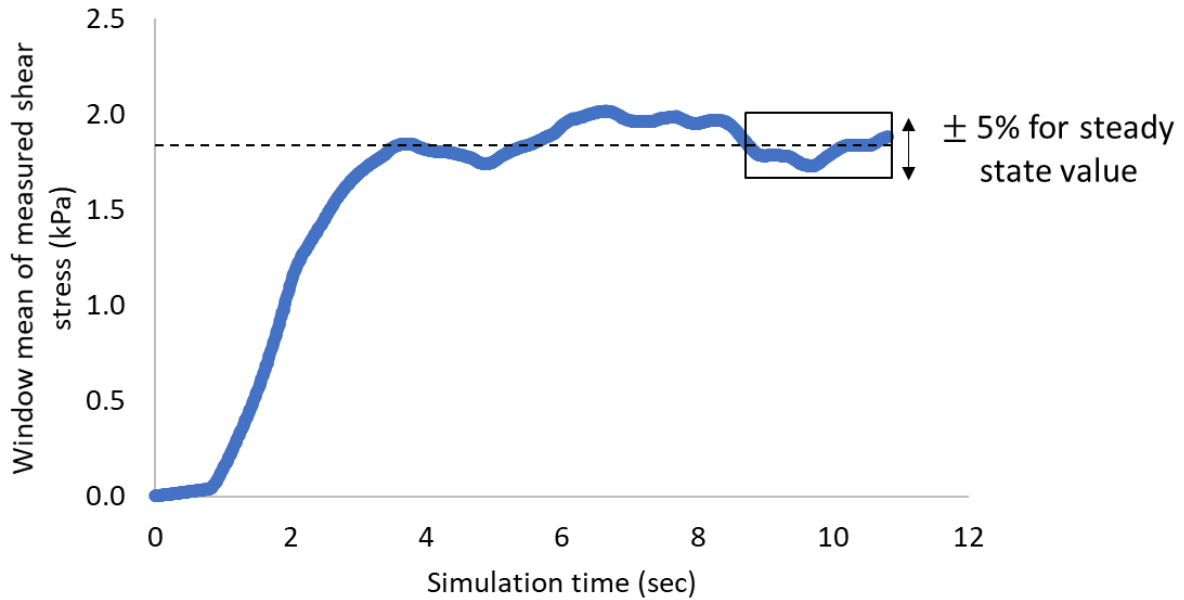
window mean calculation across 100 datapoints which is 1 second of simulation data is done and the new smoother data is used for further calculation.

An example of raw data that has been post-processed using the window mean method is shown in Figure 5.2. To get the steady state value for the first measurement of the incipient yield or for the critical state measurement, the final 2 seconds are checked for convergence within 5%. To get the maximum value for the remaining measurements of the incipient yield, the maximum value in the smoothed data set is chosen. Although this method underpredicts the maximum value due to averaging across points, it is essential to get rid of extreme fluctuations that can severely affect the final results. This steady state value and the maximum shear stress values are then tabulated to get the incipient yield locus and the critical state internal friction angle by comparing it to the normal stress. The incipient yield locus is linearly approximated to get the values for the incipient yield internal friction angle and the bulk cohesion.

DEM simulations can be sensitive to the initial particle fill or the way the particles pack based on how they are generated in the simulation. This combined with EDEM particle factories generating particles at random positions can result in non-repeatable measurements. Thus, at the start of the study, four random sets of parameter values were tested with a unique particle fill and their results were compared to each other. A set of 3 simulations were run for each of the four cases for a total of 12 simulations. The final bulk response results were within 5% of each other and going forward, only one simulation per one parameter set was run. These duplicate results were not included in any of the analysis that follows.



(a)



(b)

Figure 5.2: Shear cell data output and processing from DEM simulations – (a) Raw top plate shear stress data outputted from the ring shear cell DEM simulations, (b) Window average of raw data across 100 data points (1 second simulation time), and range for the steady state value calculation

6. CALIBRATION METHODOLOGY AND VALIDATION RESULTS

6.1 Predictive Models

The results from the shear cell simulations were analyzed using factorial analysis. The effects of each individual design of experiment parameter and interaction effects between parameters on the shear cell response were then calculated. Regression is then performed on these datapoints to generate a predictive model using only the statistically significant parameters. First, the visual representation of the main effects is shown followed by the explanation of the statistical analysis and the predictive model creation.

The main effects showcase how each parameter affects the bulk responses individually and the width of the range of values for the bulk responses for a change in any of the other parameters. This can be visually represented using a box and whisker plot. The box and whisker plot is used to represent the main effects to get a better idea of the spread of the data points and analyze the extent of outliers. The interaction effects are better represented numerically through the statistical analysis, but a visual can be shown using line plots as well.

Box and whisker plots are used to highlight five statistical data points using one plot (Williamson et al., 1989): the minimum, the maximum, the median, the first quartile, and the third quartile as shown in Figure 6.1. In addition to the usual five datapoints, a mean can also be represented on the box plot using an 'x' marker. The interquartile range is characterized by the data points in between the first and the third quartile. The minimum and maximum fences are calculated using this interquartile range value and the quartiles. The datapoints outside the interquartile range but within the minimum and maximum fences are considered mild outliers whereas datapoints outside the minimum and maximum fences are considered extreme outliers.

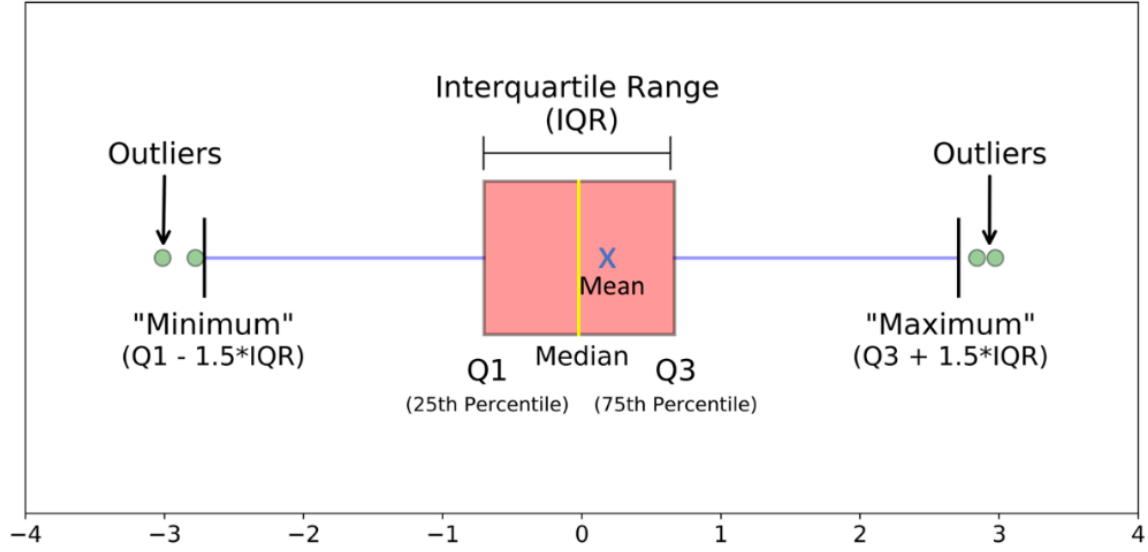


Figure 6.1: Example of a box plot with all appropriate data points represented

The benefit of using a design of experiments approach is that interaction effects can be analyzed effectively. Interaction effects are the effects that can potentially show up in analysis of real behavior where the independent variables might interact with each other. Since this behavior cannot be captured by the main effects, it is important to incorporate this behavior in a predictive model for higher model accuracy and better results. In this study, the interaction order is restricted to two parameters at a time, but higher order interaction effects can also appear in complex particle behavior modeling.

The interaction effects can be visually represented as shown in Figure 6.2, which shows the interaction effects for the DEM bulk cohesion prediction. Parameters with no significant interaction effects will show behavior similar to other combinations of the two parameter values as shown in the top left plot in Figure 6.2 with the particle size distribution $\left(\frac{\sigma_d}{d}\right)$ parameter and applied end point normal stress to the effective elastic modulus $\left(\frac{\sigma_{end}}{E'}\right)$ parameter. Parameters with significant interaction effects will have behavior different from other combinations of values for the same two parameters. This can be seen in the bottom right plot with dimensionless particle-particle cohesive surface energy density $\left(\frac{\gamma_{pp}}{E'd}\right)$ and particle-particle sliding friction (μ_{pp}) behavior. Although the visual representation gives a good indicator

of which parameters might be significant, it is not possible to gauge the numerical and statistical magnitude of the sensitivity of the final bulk response to each parameter interaction.

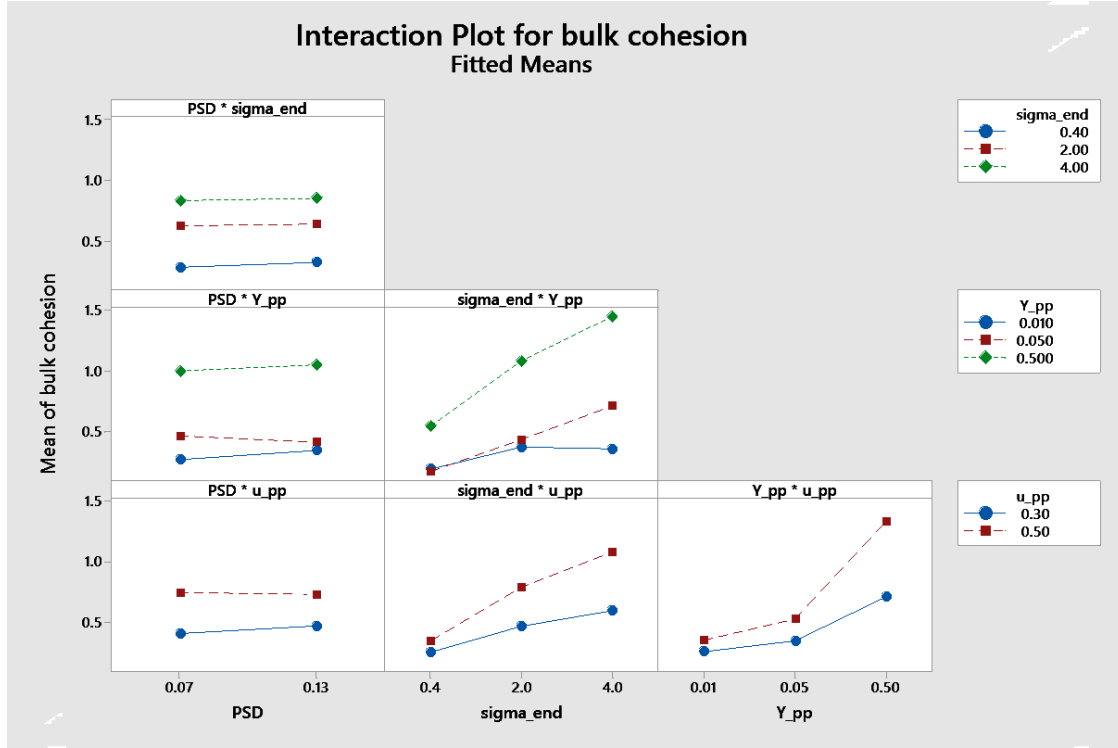


Figure 6.2: Interaction effects for combination of parameters in pairs on the bulk cohesion response of a simulated annular shear cell, where, sigma_end refers to σ_{end} , PSD refers to $\left(\frac{\sigma_d}{d}\right)$, Y_pp refers to γ_{pp} and u_pp refers to μ_{pp}

The main and interaction effects can be numerically calculated using a factorial analysis on the design of experiments simulation results. This is done using a Multivariate Analysis of Variance (MANOVA) (Bray and Maxwell, 1985; Weinfurt, 1995) table by calculating the p-values for each main and interaction effect. Any p-value larger than the significance level chosen is considered statistically significant and, thus, will be a part of the predictive model equation. For this study, the significance level chosen is $p = 0.05$ or 5%.

6.1.1 Incipient Internal Friction Angle

The main effects of all the parameters on the incipient internal friction angle (ϕ_{inc}) are represented in Figure 6.3. The median (shown with a horizontal line) and the mean (shown with an x) represent how the incipient internal friction angle (ϕ_{inc}) changes with changes in individual

parameters, whereas the interquartile range band shows the interaction effects that each individual parameter has with the remaining three parameters. All the points on the plots represent datapoints and the points outside the interquartile range (represented by bars) correspond to outliers. For particle-particle sliding friction (μ_{pp}), the change in median and mean is significant, and the interquartile range band is thin, which shows that the incipient internal friction angle (ϕ_{inc}) is significantly dependent on particle-particle sliding friction (μ_{pp}) as a parameter individually. The other three parameters do not show similar behavior. Thus, it can be inferred that in the range of values chosen, the incipient internal friction angle should be unaffected by the remaining three parameters ($\frac{\sigma_d}{d}$, $\frac{\gamma_{pp}}{E'd}$, and $\frac{\sigma_{end}}{E'}$) individually. This result will be further substantiated by the statistical analysis.

The interaction effects will be considered using the regression analysis as represented using the Pareto chart in Figure 6.4. The Pareto chart (Mathews, 2005) shows the absolute value of the standardized effects for each of the main effects and interaction effects to an order of two. The absolute value is representative of how the response is affected by each parameter, but not whether it increases or decreases the response. The red line at 2.120 represents the significance level cutoff for a significance level of 0.05, and terms with a standardized effect larger than that value are considered statistically significant.

The individual effect of the particle-particle sliding friction (μ_{pp}) and the interaction effect between the particle-particle sliding friction (μ_{pp}) and dimensionless particle-particle cohesive surface energy density term ($\frac{\gamma_{pp}}{E'd}$) are statistically significant. Thus, for the range of values chosen and using the parameters, we can predict the incipient internal friction angle using the following empirical model:

$$\phi_{inc} = b_1(\mu_{pp}) + b_2\left(\frac{\gamma_{pp}}{E'd}\right)(\mu_{pp}) \quad Eq. 6.1$$

Where b_1 and b_2 are unknown coefficients specific to the material.

The calculation methodology of these unknown coefficients is described after all three bulk response models are presented. The model shown in Equation 6.1 and the models that follow are applicable only over the range of the simulated parameter values. It is possible that another model may be appropriate over a different region of the same parameter space. This is the result of

different parameters being statistically significant over a different range of simulated parameter values leading to a different predictive model.

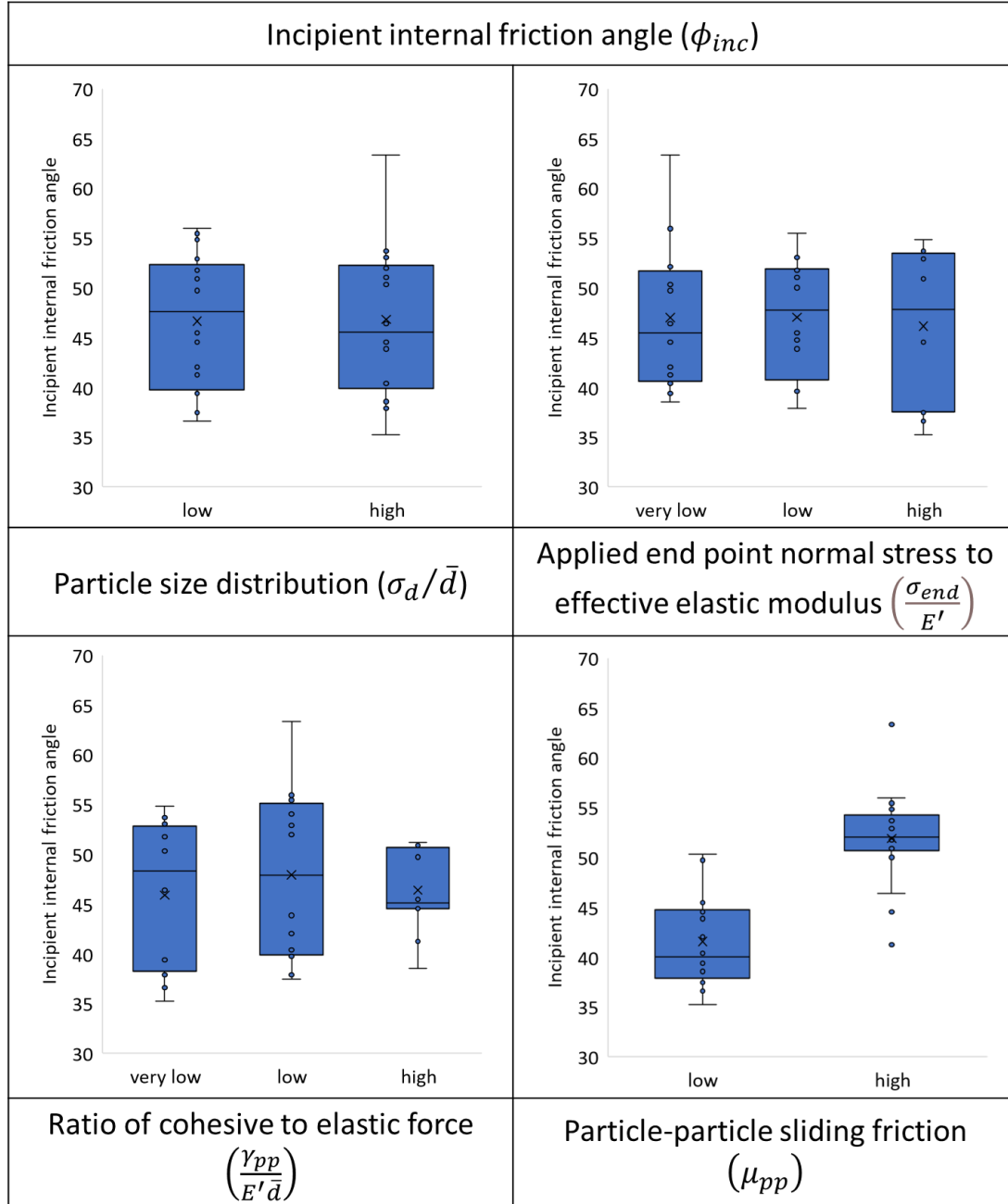


Figure 6.3: Main effects of each design of experiments parameter on the incipient internal friction angle, the values corresponding to very low, low, and high for each parameter can be found in Table 5.4

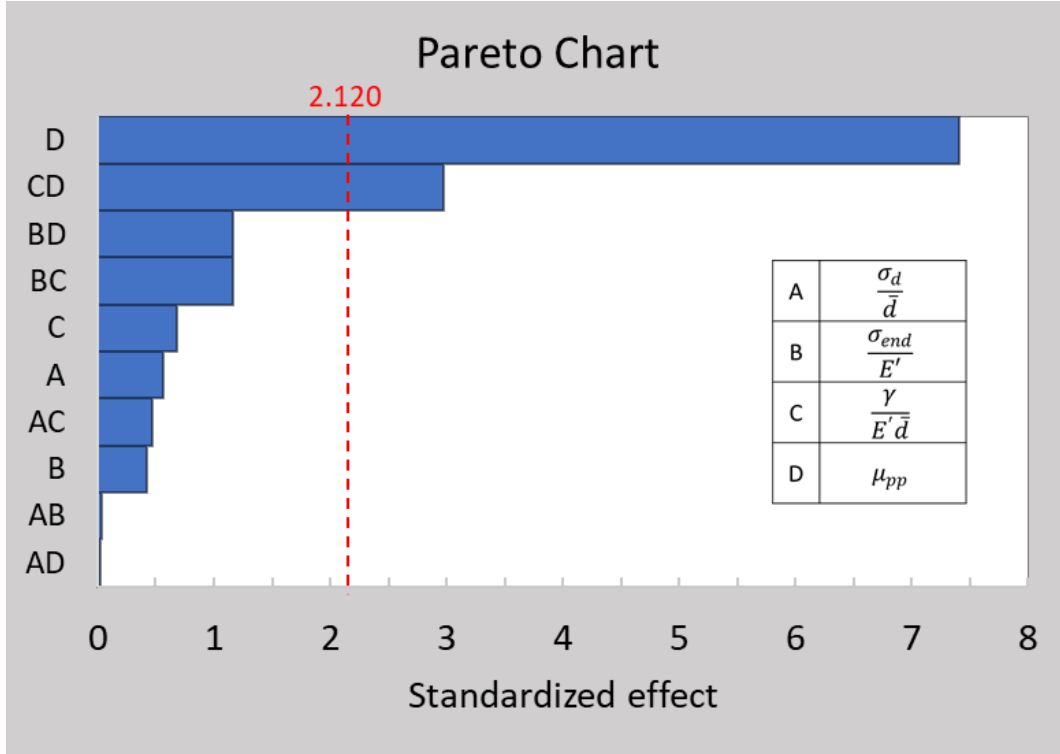


Figure 6.4: Pareto chart showing standardized effects for all terms for incipient internal friction angle response of a simulated annular shear cell.

6.1.2 Critical State Internal Friction Angle

The main effects of all the parameters on the critical state internal friction angle (ϕ_{crit}) are represented in Figure 6.5. For the particle size distribution parameter, the change in the median and mean does not affect the critical state internal friction angle (ϕ_{crit}) significantly, at least over the range of values investigated here. The remaining three parameters show a significant change in the median and mean with a change in their values and, thus, could be a factor in the model. The particle-particle sliding friction (μ_{pp}) has a thin interquartile range bar along with a noticeable change in values of the median and means. Thus, μ_{pp} should especially be one of the significant factors in the model.

The Pareto plot in Figure 6.6 shows that the individual main effects for all the parameters, except the particle size distribution parameter, are statistically significant. In addition to the main interaction effects, the interaction effect between the particle-particle sliding friction (μ_{pp}) and dimensionless particle-particle cohesive surface energy density term ($\frac{\gamma_{pp}}{E' \bar{d}}$) is also

significant. Thus, for the range of values chosen and using the parameters, we can predict the critical state internal friction angle using the following model:

$$\phi_{crit} = d_1(\mu_{pp}) + d_2\left(\frac{\sigma_{end}}{E'}\right) + d_3\left(\frac{\gamma_{pp}}{E'\bar{d}}\right) + d_4(\mu_{pp})\left(\frac{\gamma_{pp}}{E'\bar{d}}\right) \quad Eq. 6.2$$

Where d_1, d_2, d_3 , and d_4 are unknown coefficients specific to the material.

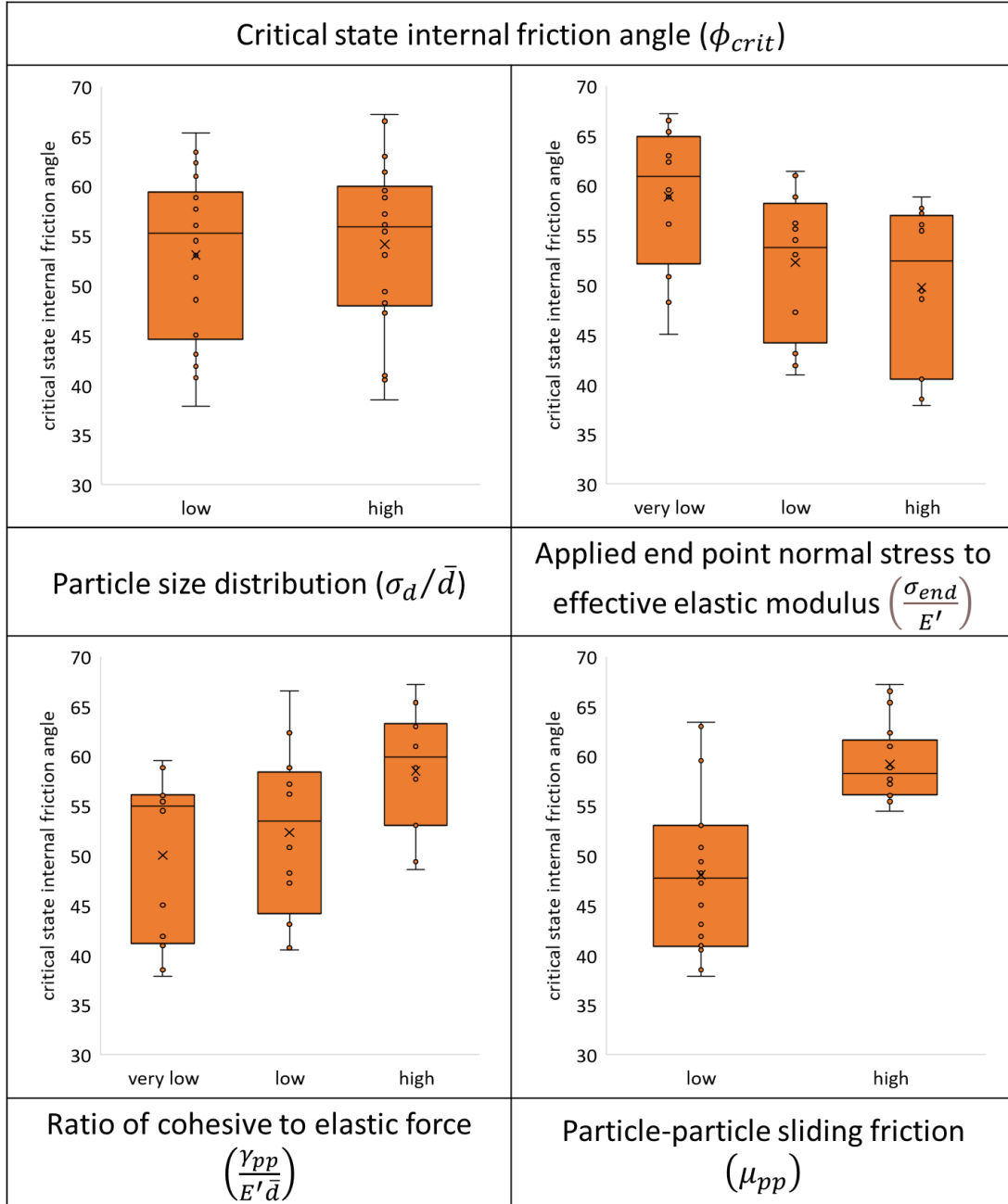


Figure 6.5: Main effects of each design of experiments parameter on the critical state internal friction angle, the values corresponding to very low, low, and high for each parameter can be found in Table 5.4

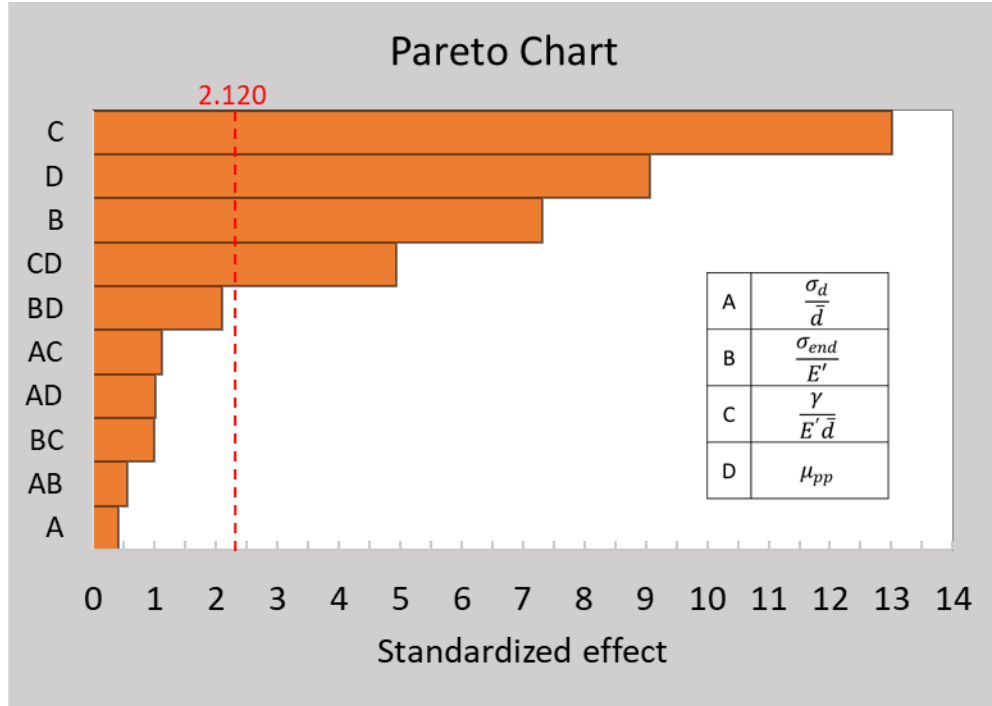


Figure 6.6: Pareto chart showing standardized effects for all terms for critical state internal friction angle response of a simulated annular shear cell

6.1.3 Dimensionless Bulk Cohesion

The main effects of all the parameters on dimensionless bulk cohesion $\left(\frac{c}{E'}\right)$ are represented in Figure 6.7. Similar to the critical state incipient internal angle, the dimensionless bulk cohesion median and mean do not show any significant change with the change in particle size distribution parameter in the value range chosen. Thus, this parameter would not be a part of the model. The other three parameters all show significant changes in the median and mode of the response and could thus be a part of the model. The dimensionless bulk cohesion response is seen to be highly dependent on the dimensionless particle-particle cohesive surface energy density term $\left(\frac{\gamma_{pp}}{E' d}\right)$ and the dimensionless end consolidation stress term $\left(\frac{\sigma_{end}}{E'}\right)$.

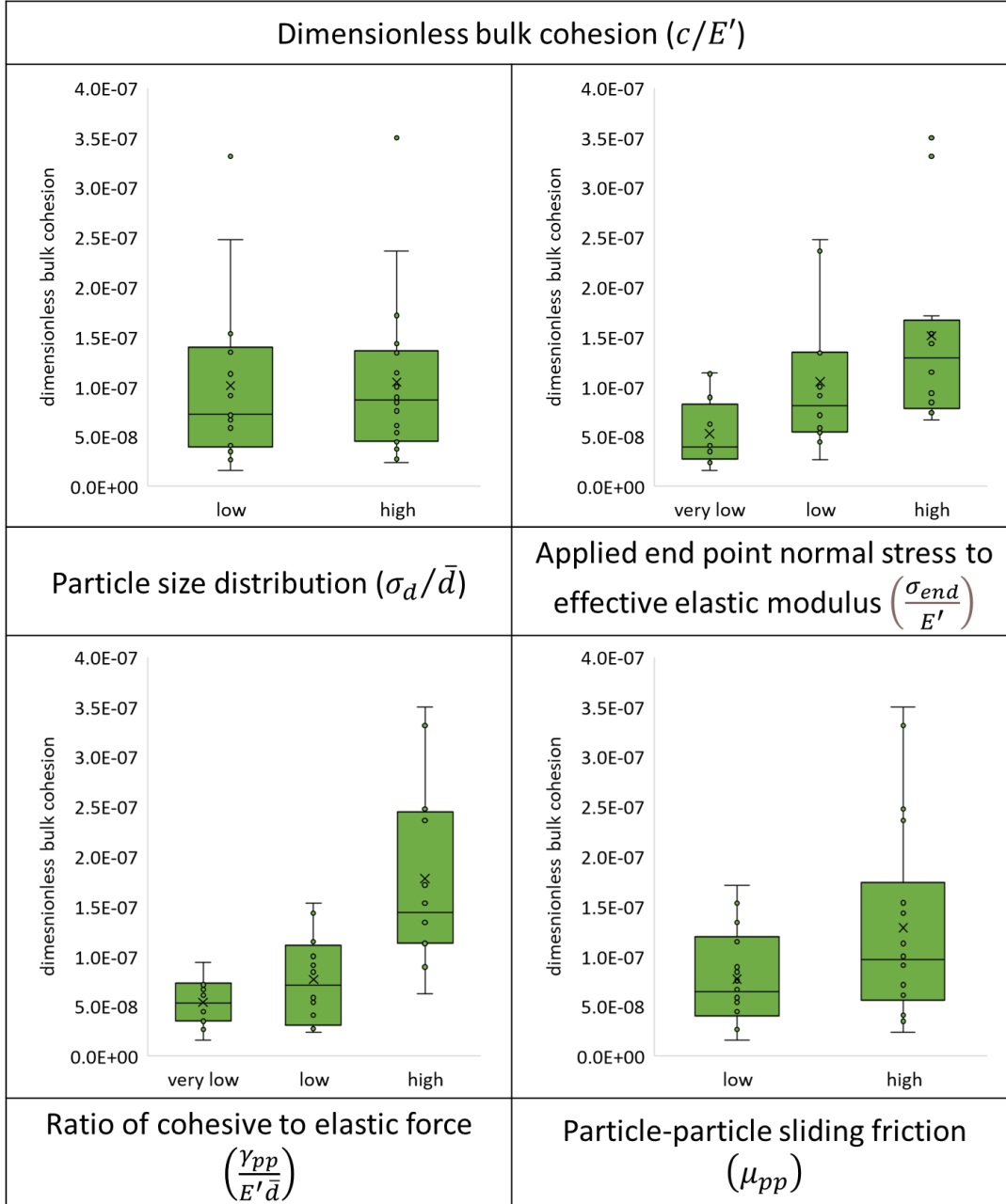


Figure 6.7: Main effects of each design of experiments parameter on the dimensionless bulk cohesion, the values corresponding to very low, low, and high for each parameter can be found in Table 5.4

The Pareto plot for dimensionless bulk cohesion in Figure 6.8 shows that individual main effects for all the parameters, except for the particle size distribution parameter, are statistically significant. The interaction effects of the dimensionless particle-particle cohesive surface energy density term ($\frac{\gamma_{pp}}{E'\bar{d}}$) with particle-particle sliding friction (μ_{pp}) and the dimensionless end

consolidation stress term $\left(\frac{\sigma_{end}}{E'}\right)$ are also observed to be statistically significant. Thus, for the range of values chosen and using the parameters, we can predict the dimensionless bulk cohesion using the following model:

$$\frac{c}{E'} = e_1 \left(\frac{\gamma}{E' \bar{d}} \right) + e_2 \left(\frac{\sigma_{end}}{E'} \right) + e_3 (\mu_{pp}) + e_4 \left(\frac{\gamma_{pp}}{E' \bar{d}} \right) (\mu_{pp}) + e_5 \left(\frac{\sigma_{end}}{E'} \right) \left(\frac{\gamma_{pp}}{E' \bar{d}} \right) \quad Eq. 6.3$$

Where e_1, e_2, e_3, e_4 and e_5 are unknown coefficients specific to the material.

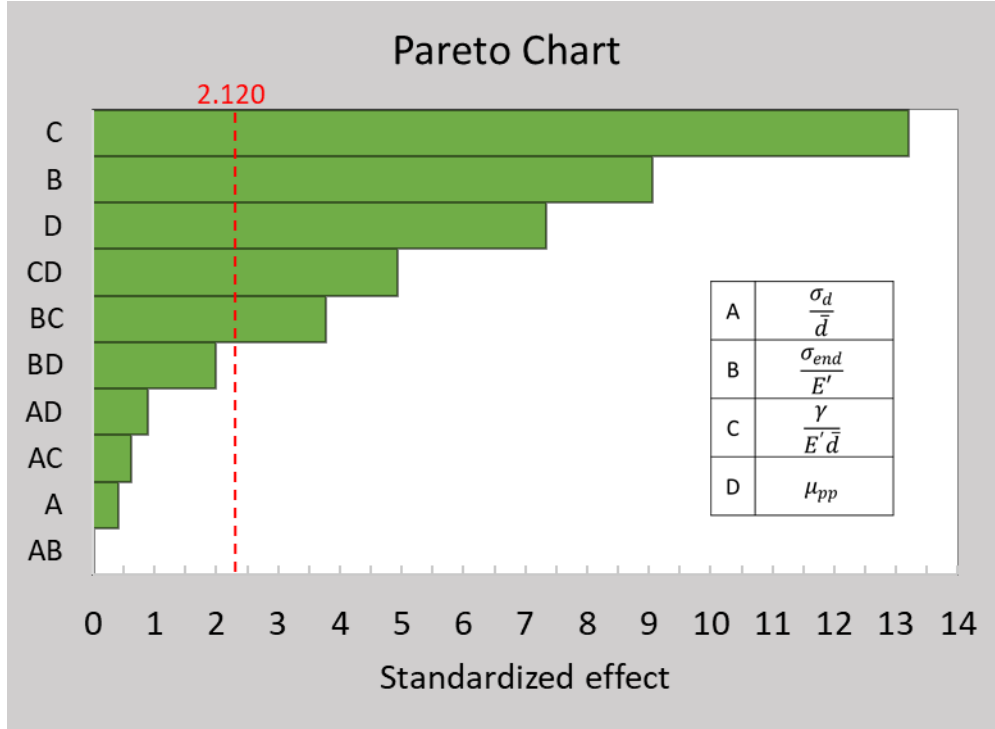


Figure 6.8: Pareto chart showing standardized effects for all terms for dimensionless bulk cohesion response of a simulated annular shear cell

The models described in equations 6.1, 6.2, and 6.3 have their respective coefficients (b_i, d_i, e_i) that can be calculated by surface fitting the equations to simulation data results. This surface fitting was done by linearly regressing the predictive model created and the data points for each simulation using the built-in MATLAB function 'regress(y, X)'. Further, as the design of experiments parameter value ranges do not cover the complete range of values for each parameter, there was a constant term added to each of the models to ensure a better fit for the coefficients in each equation.

6.2 Parameter Correlation

The predictive models found using the DEM shear cell simulations will be ideally used to calibrate for particle parameters. This is not possible if there is a strong interdependence or correlation between any of the parameters being used for calibration. Thus, to avoid such an issue, the parameters were checked for any correlation. For each parameter set, the values found for each of the bulk responses were plotted against another to see if there is a significant trend to be seen. The correlation plot between incipient internal friction angle and dimensionless bulk cohesion is shown in Figure 6.9 and the incipient internal friction angle and the critical state internal friction angle correlation plot is shown in Figure 6.10.

There is no significant correlation between the dimensionless bulk cohesion and the incipient internal friction angle. This was done quantitatively by trying to fit multiple typical models to the data points, but all models resulted in statistically insignificant R-squared values. Thus, it was concluded that there is no correlation between the two parameters. Since there is no correlation, the two parameters can be used together in a calibration effort. The two internal friction angles have a linear correlation and thus the two cannot be used together for calibration. Now, the models modeling these two parameters as given by Equation 6.1 and Equation 6.2 are not identical. The two parameters do not necessarily need to have an identical form because they are correlated. As these parameter values are two distinct quantities, the offset between the two can be explained by these different terms. The correlation between them can be seen in their models by their shared terms which are (μ_{pp}) and $\left[\left(\frac{\gamma_{pp}}{E'd}\right) \cdot (\mu_{pp})\right]$.

This linear relationship between the two internal friction angles has been previously looked at by Bolton's (1986) work on the strength and dilatancy of sands. They reported the relationship between the two internal friction angles for quartz sand using the angle of max dilation (ψ_{max}) and a constant value (α) dependent on the material as shown in Equation 6.4.

$$\phi_{crit} - \phi_{inc} = \alpha \cdot (\psi_{max}) \quad Eq. 6.4$$

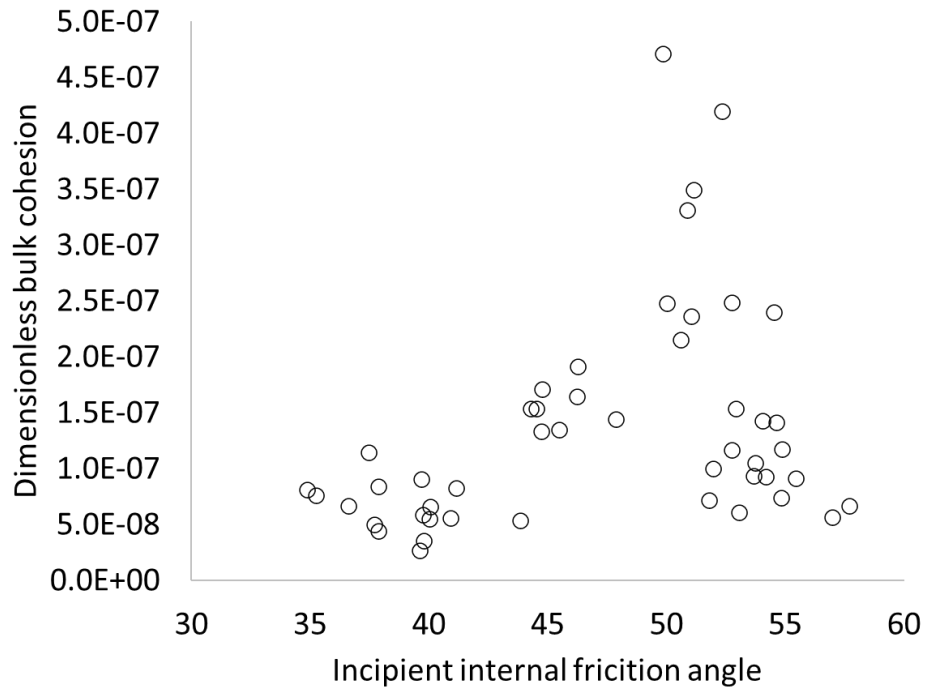


Figure 6.9: Correlation between incipient internal friction angle and dimensionless bulk cohesion

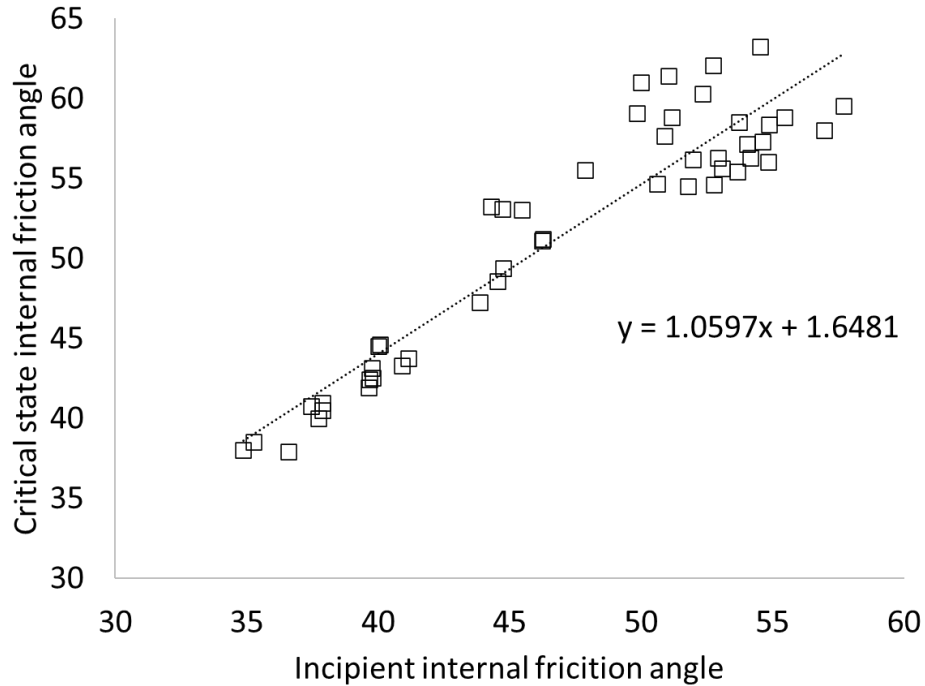


Figure 6.10: Correlation between incipient internal friction angle and critical internal friction angle

6.3 Model Optimization

The predictive models for the incipient internal friction angle (ϕ_{inc}), the critical state internal friction angle (ϕ_{crit}), and dimensionless bulk cohesion ($\frac{c}{E'}$) are incomplete without the values of the coefficients. These values can be found by surface fitting the model to the DEM simulation data. As mentioned earlier, this was done using a simple linear regression using the in-built MATLAB function ‘regress(y, X)’. The surface fit was restricted to an R-squared value greater than 0.95 to maintain the significance level chosen previously. The resulting equation then would be a function dependent only on the values of the design of experiments parameters and bulk response predictions can be made using these final models. Since the interest was in calibrating for material parameters like $\frac{\gamma_{pp}}{E'\bar{d}}$ or μ_{pp} and not the experimental parameters like $\frac{\sigma_{end}}{E'}$, the surface fit was done for a fixed value of σ_{end} . The work and discussion going forward will be for individual σ_{end} values. The surface plot for dimensionless bulk cohesion ($\frac{c}{E'}$) at σ_{end} value of 2kPa with an R-squared value of 0.98 is shown in Figure 6.11 for the two material parameters, $\frac{\gamma_{pp}}{E'\bar{d}}$ and μ_{pp} , along with the individual points highlighted in blue.

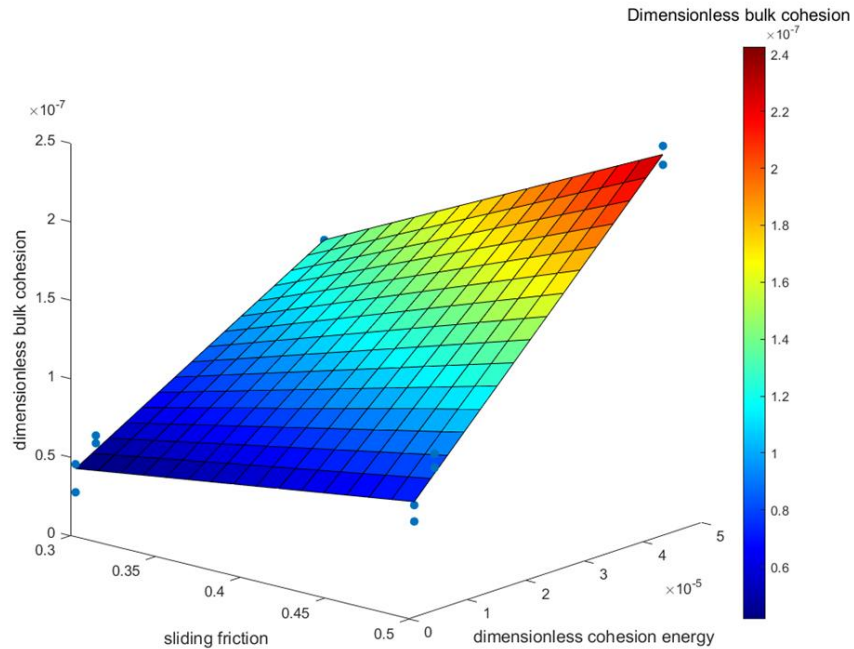


Figure 6.11: Surface plot representing the fitting of the predictive model from equation 6.3 with the dimensionless bulk cohesion simulation data at 2kPa represented as blue dots

The fitting-parameters and the model equation together is the prediction for each of the three response parameters for specific values of the design of experiments parameters. These material parameter values differ for different materials and need to be found using calibration via optimization. For optimization, objective functions were created for the two response parameters, ϕ_{inc} and $\frac{c}{E'}$, is used in calibration. These objective functions were defined as the absolute relative error between the experimental measurements and the predictive model created as shown in Equations 6.5 and 6.6. Here, the DEM predictions, $(\phi_{inc})_{DEM}$ and $\left(\frac{c}{E'}\right)_{DEM}$, are functions of μ_{pp} and $\frac{\gamma_{pp}}{E'd}$ at a certain fixed σ_{end} value. The experimental values, $(\phi_{inc})_{exp.}$ and $\left(\frac{c}{E'}\right)_{exp.}$, are the average numerical value of all experimental measurements taken at the same σ_{end} value using the shear cell for the material being calibrated for.

$$Obj_1 = \frac{((\phi_{inc})_{DEM} - (\phi_{inc})_{exp.})_{abs}}{(\phi_{inc})_{exp.}} \quad Eq. 6.5$$

$$Obj_2 = \frac{\left(\left(\frac{c}{E'}\right)_{DEM} - \left(\frac{c}{E'}\right)_{exp.}\right)_{abs}}{\left(\frac{c}{E'}\right)_{exp.}} \quad Eq. 6.6$$

The three powder samples tested are lactose, (hydroxypropyl) methyl cellulose (HPMC), and ABT-089. The apparent particle density of each powder was measured using the Micromeritics AccuPyc Helium pycnometer, and the poured and tapped bulk density (after 600 taps) was measured using an Agilent tapped bulk density tester. The experimental values for all these density measurements are summarized in Table 6.1. Although the density of the powders was measured, in the DEM simulations a fixed density of 1.0 g/cm³ or 1000 kg/m³ was used. A fixed value was chosen for the density throughout the simulations since the density was not a factor to be varied in the design of experiments set up nor does it play a role in the shear cell simulations. The average particle diameter measurements for lactose, HPMC, and ABT-089 as measured using the Mastersizer 3000 by laser diffraction were 19.1 μ m, 15.9 μ m, and 10.6 μ m respectively

In addition to the density measurements, the incipient yield and critical state behavior of the three powder samples was measured using a Schulze ring shear cell tester RST-XS. The bulk responses measured using the shear cell were the incipient internal friction angle, critical state internal friction angle, and the bulk cohesion. The experimental values for all the shear cell measurements are summarized in Table 6.2.

Table 6.1: Summary of experimental density measurements for lactose, HPMC, ABT-089

Sample Name	Apparent density (g/cm ³)	Poured bulk density (g/cm ³)	Tapped bulk density (g/cm ³)
Lactose	1.65	0.424	0.657
HPMC	1.34	0.329	0.481
ABT-089	1.43	0.330	0.473

Table 6.2: Summary of experimental shear cell measurements at different end consolidation stresses for lactose, HPMC, ABT-089

Sample Name	σ_{end} (kPa)	ϕ_{inc} (deg)	Bulk cohesion (c) (kPa)	ϕ_{crit} (deg)
Lactose	0.4	31.7	0.164	43.7
	2	34.7	0.461	40.8
	4	34.7	0.930	41.3
HPMC	0.4	42.5	0.0565	45.0
	2	46.7	0.263	49.1
	4	45.7	0.408	47.4
ABT-089	0.4	42.9	0.140	47.5
	2	38.2	0.602	46.1
	4	38.4	1.04	45.0

These objective functions were subject to a genetic algorithm for multiple-objective optimization with constraints on the parameter values until the model converges with a given residual value. This optimization was done using the in-built MATLAB optimization tool and the ‘gamultobj’ function. The success of the calibration effort was measured using the final value of these two objective functions. The residual value was chosen to be 5% in accordance with the previous significance levels. In addition to the convergence residual error value, the lowest error was set to 0.01% to reduce computational time. The constraints were put in place to ensure non-negativity and large magnitude limits on the parameter values being varied by the algorithm. The values at which the optimization algorithm converges within the residual values for both functions are the calibrated values for the parameters at that σ_{end} value.

The calibrated parameter values found using ϕ_{inc} and $\frac{c}{E'}$ models were then tested with a DEM simulation for ϕ_{crit} to get partial validation results. The success of the partial validation was measured using residual error as well. Since there is a degree of correlation between the two internal friction angles, the partial validation cannot be used as a reasoning for calibration success, but it serves as a quick indicator during the modeling phase of the work. Later validation using an independent experiment was conducted to confirm and validate the calibration effort. The calibration residual error and partial validation error results for the optimization are summarized in Table 6.3.

The calibration and partial validation error results for both the lactose and the ABT-089 powder sample results were within the significance level chosen (<5%). Hence, the calibrated values for these two powder samples can be used for independent validation directly. The HPMC powder sample consistently had high calibration errors and a resulting high partial validation error for the current set of parameters. This result shows that the powder flow behavior of HPMC was not being captured completely with the set of parameters or the range of values in the model. The powder sample was thus investigated further.

Table 6.3: Summary of calibration and partial validation error results

Sample Name	σ_{end} (kPa)	Calibration error % for μ_{pp}	Calibration error % for $\frac{\gamma_{pp}}{E'd}$	Partial validation error %
Lactose	0.4	0.01%	0.01%	1.42%
	2.0	0.01%	0.01%	1.62%
	4.0	0.01%	0.01%	0.56%
HPMC	0.4	~17%	~15%	18.42%
	2.0	~14%	~13%	12.49%
	4.0	~14%	~13%	13.89%
ABT-089	0.4	0.01%	~1%	2.78%
	2.0	0.01%	~1%	2.28%
	4.0	0.01%	~1%	1.72%

6.4 Modification for HPMC: Addition of particle shape factor

HPMC particles have been previously characterized as fiber-like particles with small particle size as shown in Figure 6.12 but a comparatively high surface area that can combine to form larger, elongated particles (Allenspach et al., 2020). This characterization directly affects the flow behavior, and the flow behavior apparently cannot be captured accurately using spherical particles in DEM. The fibrous HPMC particles were modeled as capsule-shaped particles with larger aspect ratios in another work by (Allenspach, 2020) to capture this behavior.

The non-spherical shape can also be replicated in DEM using the glued-sphere approach which is also referred to as the multi-sphere approach (Gallas and Sokolowski, 1993; Kodam et al., 2009; Nolan and Kavanagh, 1995; Ristow, 1994). In the glued-sphere approach, a non-spherical particle is modeled as multiple particles fused together to create the same shape. This makes sure that the spherical contact models can be continued to be used while also replicating the more complex shape. Thus, to ensure better model calibration for the HPMC powder measurements, the DEM design of experiments simulations were repeated with capsule-shaped particles with an increased aspect ratio (A_r) of two. These particles were also not allowed to rotate similar to previous spherical particles. This is not the typical approach taken when modeling non-spherical particles. If the particles have irregular shapes, the actual particle shape accounts for their resistance to rolling. The spherical particles not being allowed to rotate is to accommodate for the deviation of the real particle shape from spheres. An individual capsule-shaped particle was modeled with five particles using the glued-sphere model in DEM as shown in Figure 6.13. The five particles in the glued-sphere model ensure that there are no sharp changes in the particle surface topography.

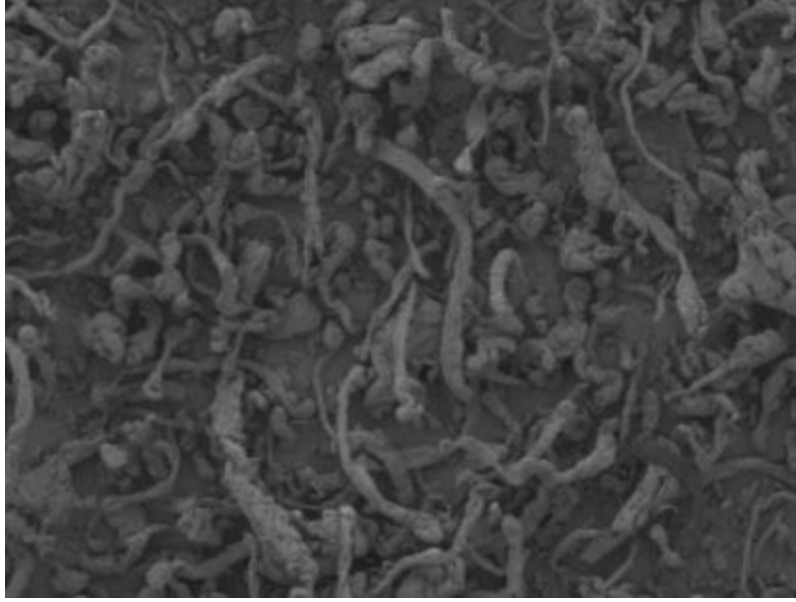


Figure 6.12: HPMC particle morphology showing fibrous particles captured by HPMC characterization work done by Allenspach et al., (2020)



Figure 6.13: Capsule-shaped particle modeled in DEM using five particles in a glued-sphere model (an individual particle part of the glued-sphere highlighted in red)

The calibration procedure was repeated including the model generation, calculating the fitting coefficients, and the optimization. The models for the three parameters, incipient internal friction angle (ϕ_{inc}), the critical state internal friction angle (ϕ_{crit}), and dimensionless bulk cohesion ($\frac{c}{E'}$), were found to be the same but with different coefficients. The calibration errors and partial validation errors for HPMC with an increased aspect ratio are summarized in Table 6.4.

Table 6.4: Updated calibration and partial validation error results for HPMC with an increased aspect ratio ($A_r = 2$)

Sample Name	σ_{end} (kPa)	Calibration error % for μ_{pp}	Calibration error % for $\frac{\gamma_{pp}}{E'd}$	Partial validation error %
HPMC ($A_r = 2$)	0.4	~2%	~3%	2.44%
	2.0	~1%	~1%	1.24%
	4.0	~0.01%	~1%	0.72%

With an updated aspect ratio value, the calibration errors and the partial validation errors for HPMC are within the significance level (5%) specified. The new calibrated values can be used for HPMC in the independent validation. The errors for HPMC are still relatively high compared to the other two samples. This suggests that including aspect ratio as another parameter for calibration could potentially increase the result accuracy. Work by Y Guo et al., (2013) investigated granular shear flow behavior of particles with non-spherical particles using DEM. In this work by Guo, the particles with friction were seen to align themselves in a preferential orientation with their largest dimensions aligned at a small angle in the flow direction. This alignment reduces the stresses and leads to better flow behavior. But at higher solid fractions before this alignment, they observed that there was a sharp increase in stress which implies a higher resistance to shearing initially. But as the particles align, they noticed that these stresses decreased.

The final calibrated values for μ_{pp} and $\frac{\gamma_{pp}}{E'd}$ for the respective σ_{end} values are summarized in Table 6.5. The calibrated values for lactose and ABT-089 are for simulations with an aspect ratio of one whereas the calibrated values for HPMC are with an aspect ratio of two. The calibrated values for μ_{pp} have minimal change with a change in the σ_{end} values for all three powder samples. The calibrated values for $\frac{\gamma_{pp}}{E'd}$ showed significant change with a change in σ_{end} values. For all three powder samples, the $\frac{\gamma_{pp}}{E'd}$ decreased with a decrease in σ_{end} as shown in Figure 6.14.

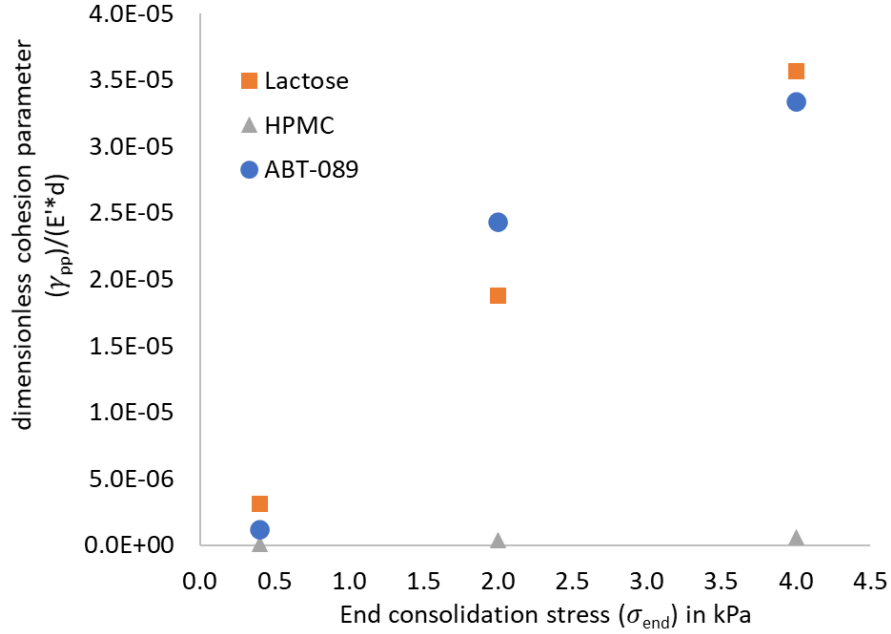


Figure 6.14: Change in the calibrated $\frac{\gamma}{E'd}$ value with a change in the end consolidation stress for all three powder samples (lactose, HPMC, ABT-089)

Table 6.5: Summary of calibrated parameter values for all three powder samples at different end consolidation stresses

Sample Name	σ_{end} (kPa)	Calibrated value for μ_{pp}	Calibrated value for $\frac{\gamma_{pp}}{E'd}$ (γ_{pp})
Lactose ($A_r=1$)	0.4	0.250	3.13E-06 (0.036 $\frac{J}{m^2}$)
	2.0	0.250	1.88E-05 (0.216 $\frac{J}{m^2}$)
	4.0	0.252	3.57E-05 (0.411 $\frac{J}{m^2}$)
HPMC ($A_r=2$)	0.4	0.311	1.04E-07 (0.0012 $\frac{J}{m^2}$)
	2.0	0.316	3.47E-07 (0.004 $\frac{J}{m^2}$)
	4.0	0.306	6.08E-07 (0.007 $\frac{J}{m^2}$)

Table 6.5 continued

ABT-089 ($A_r = 1$)	0.4	0.300	$1.22\text{E-}06 \text{ (}0.014 \frac{J}{m^2}\text{)}$
	2.0	0.295	$2.43\text{E-}05 \text{ (}0.280 \frac{J}{m^2}\text{)}$
	4.0	0.304	$3.34\text{E-}05 \text{ (}0.385 \frac{J}{m^2}\text{)}$

6.5 Validation using Flodex Tester

The DEM simulation setup for the Flodex mimicked the experimental procedure. The funnel opening was duplicated by using a particle factory at the top of the simulated cylinder. The particle diameter of 2 mm as used previously is close to the diameters used for the disks in the Flodex and would have led to mechanical arching as shown in Figure 6.15. To avoid mechanical arching issues in DEM, the particle diameter was reduced to 1 mm from 2 mm. Since the dimensional analysis approach was used in the calibration, the individual parameters were free to be varied as long as the calibrated dimensionless values were the same. The calibrated dimensionless parameters and all the remaining dimensionless parameter values were kept constant by changing other parameters to offset the change in the particle diameter.

The calibrated dimensionless cohesion value is dependent on the end consolidation stress value which relates to the stress the powder particles experience. Since experiments unlike the shear cell, like the Flodex, do not have direct measurements of stress on the particle bed, the stress value on the particles has to be approximated. For the Flodex, the stress value corresponding to the calibrated parameter value was found using the hydrostatic pressure at the bottom layer of the particle bed. The known calibrated values of $\frac{\gamma_{pp}}{E'd}$ were found at σ_{end} values of 0.4 kPa, 2 kPa, and 4 kPa. Any value between these values can be found using the values acquired. The hydrostatic pressure was found directly using EDEM after the particle bed had settled, using this value the specific calibrated value was found by interpolation. The results of the validation using the calibrated DEM parameter values are summarized in Table 6.6.

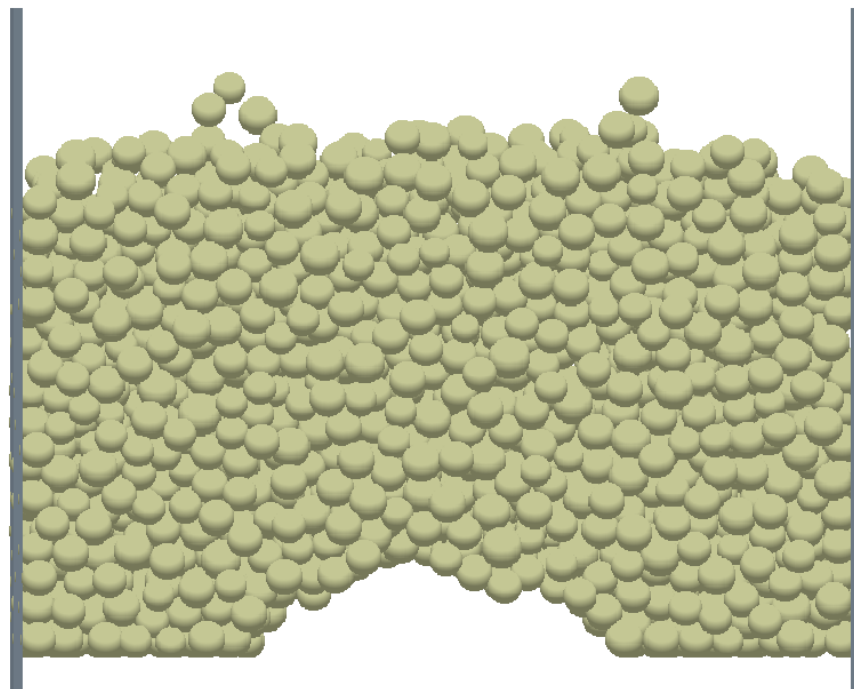


Figure 6.15: Flodex DEM simulation (without cohesion) slice showing mechanical arching for larger particle diameter for particle diameter to orifice diameter ratio of 12

Table 6.6: Summary of Flodex experimental measurements and simulation results

Sample Name	Flodex Flowability Index	
	Experimental Measurements	DEM Simulations
Lactose	28	30 ($A_r = 1$)
HPMC	22	20 ($A_r = 2$)
ABT-089	34	34 ($A_r = 1$)

The calibrated model predicted the Flowability index results with success. The lactose and HPMC Flowability index predictions were off by one disk diameter increment. The calibrated model overpredicted the Flowability index for one of the simulations with an aspect ratio of one

and it underpredicted the Flowability index for the simulation with an aspect ratio of two. This result suggests that the increased aspect ratio particles have a better simulated flow as shown by the lower Flowability index. The initial fill and the final success for HPMC with non-spherical particles with an aspect ratio of two can be seen in Figure 6.16.

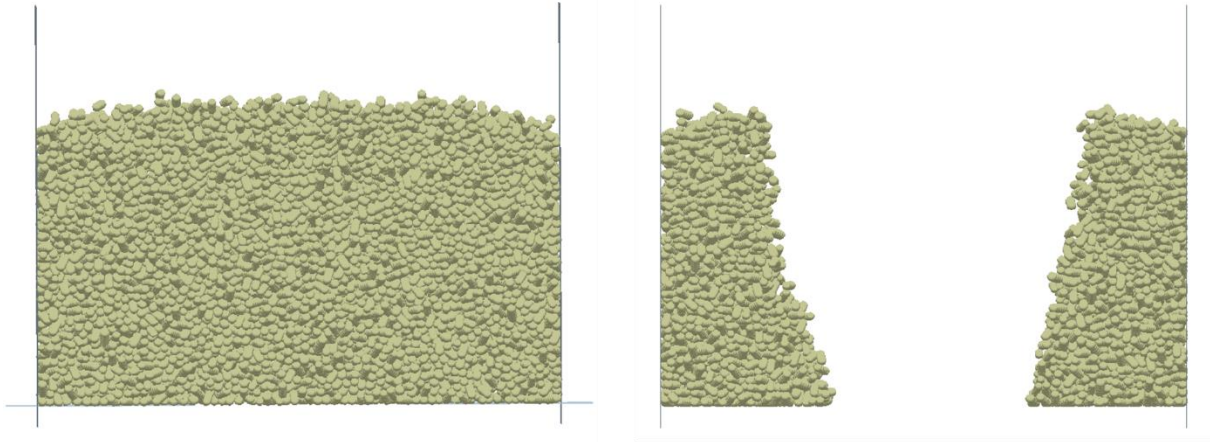


Figure 6.16: HPMC DEM simulation slice showing the particle fill (left) and one of the final successful passes (right) for particles with non-spherical shapes

A sensitivity analysis was performed based on the factory size and location. This sensitivity analysis was done to ensure the particles are not packing in a specific way due to the factory geometry in the original factory. Two additional cases were tested against the original DEM particle factory. The initial factory, referred to as factory 1, had a radius equal to the inner diameter of the Flodex and was aligned with the top opening of the Flodex. For factory 2, this diameter was halved and for factory 3, factory 2 was raised 2 cm above the Flodex top surface. The three factories are visually shown in Figure 6.17. The 2 cm distance was chosen to reproduce the actual distance of the funnel in the experimental measurement. The results of the sensitivity analysis are summarized in Table 6.7.

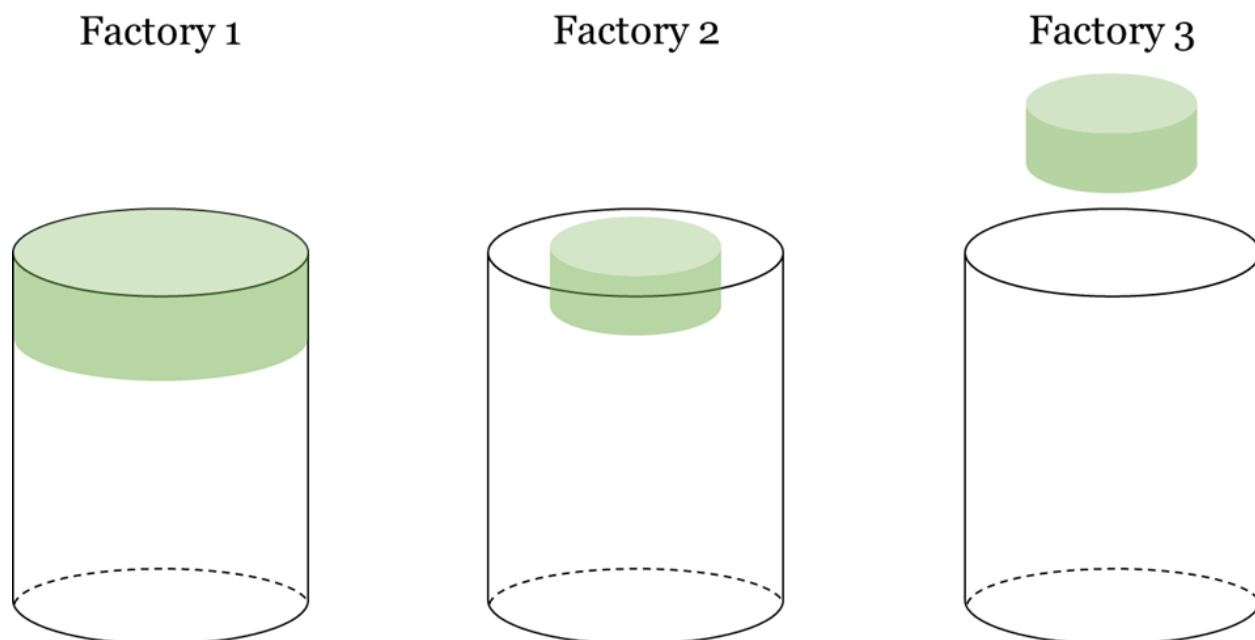


Figure 6.17: The three separate factory cases tested in the factory radius and height sensitivity analysis

Table 6.7: Summary of results for the Flodex factory sensitivity study

Sample Name	Flodex Flowability Index			
	Experimental Measurements	DEM Simulations (Factory 1)	DEM Simulations (Factory 2)	DEM Simulations (Factory 3)
Lactose	28	30 ($A_r = 1$)	32 ($A_r = 1$)	32 ($A_r = 1$)
HPMC	22	20 ($A_r = 2$)	20 ($A_r = 2$)	20 ($A_r = 2$)
ABT-089	34	34 ($A_r = 1$)	34 ($A_r = 1$)	34 ($A_r = 1$)

As the summarized results suggest, the Flodex Flowability index measurement as simulated by DEM is not highly sensitive to the factory size or factory height up to 2 cm. The

decreased factory size and increased factory height resulted in minor changes for lactose and no change for the other two powder samples. The reason for the minor change for lactose is due to mound formation on the powder free surface for smaller factory diameter. This was also seen in the other two powder samples as well, an example from ABT-089 is shown in Figure 6.18 and the resulting failure due to it in Figure 6.19. This sort of mound formation was also seen in the experiments performed but to a significantly lower extent. The large mound formation could be a result of a larger DEM particle diameter compared to real powder particles. Since the ratio of the powder diameter to the funnel height is significantly higher in the case of DEM particles compared to the measurements with real powder, it might have resulted in formations of these larger mounds.

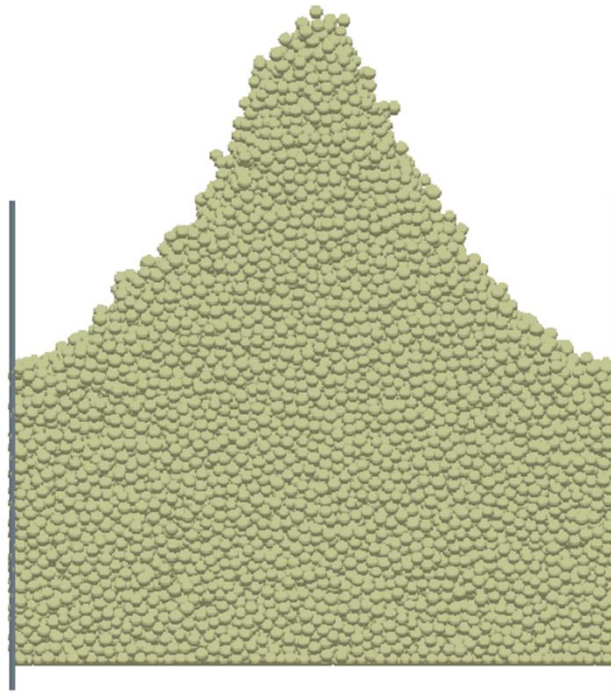


Figure 6.18: Flodex DEM simulation showing larger mound formation for ABT-089 for smaller factory diameters

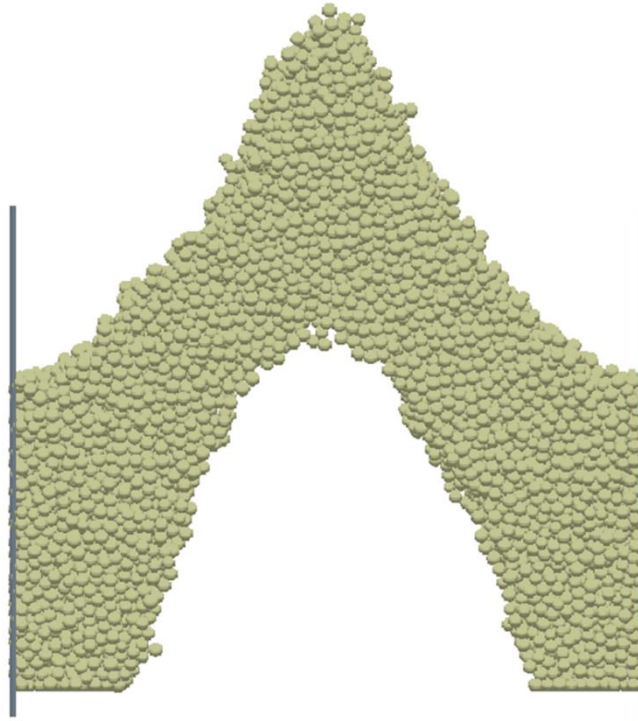


Figure 6.19: Flodex DEM simulation showing the resulting failure due to the high mound formation causing extensive arches for ABT-089 at a disk diameter of 32mm

Lower factory diameters were not explored in this sensitivity analysis as at lower particle diameters, the EDEM factories would start jamming. The particles would start piling up due to high cohesion until the particle column reached the factory. This resulted in the factory volume being completely covered by already generated particles leaving no room for new particles to be generated. A slice from a simulation case with a factory diameter quarter of the Flodex inner diameter is shown in Figure 6.20. The slice is across the center of the Flodex during the filling step with the factory highlighted in cyan. As mentioned previously, the particle column of the cohesive material built upon itself to clog to factory leading to no new particles being generated, and thus the simulations had to be halted.

It is important to note that there will be additional parameters of significance for the Flodex. For example, particle density does not play a significant role in the shear cell simulations, but it can play a role in the Flodex simulations. Since this density is not calibrated for the particles being modeled, it can certainly affect the validation results. The current Flodex simulation results predicted the Flowability index values with success with a fixed value of density. But it should be

expected that the Flodex system is sensitive to the particle density as a DEM input parameter. Thus, the Flodex system should have an additional dimensionless parameter of $\frac{\rho g \bar{d}^2}{\gamma_{pp}}$ to better capture the inertial effects. This parameter was not necessary for the shear cell due to the unimportance of gravity and inertial effects in that system.

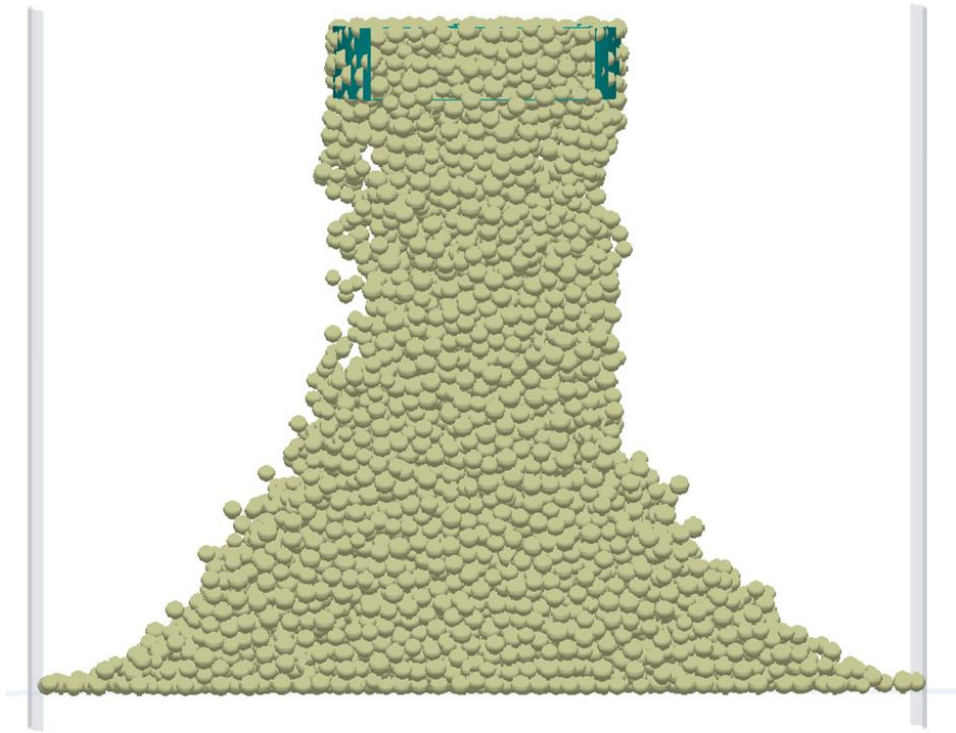


Figure 6.20: Flodex DEM simulation slice showing clogging of factories for lower factory sizes with the particle factory highlighted in cyan at the top

This additional dimensionless parameter $\frac{\rho g \bar{d}^2}{\gamma_{pp}}$, also referred to as the Bond number, was not investigated in the analysis, but the validation using the Flodex was still successful. The shear cell simulations were expected to be not sensitive to density as was confirmed by preliminary simulations and prior DEM experience. So, the value chosen for density in the shear cell simulations did not affect the results. But successful validation using the Flodex without density scaling was unexpected as the Flodex simulations were expected to be sensitive to the density values. This validation result was further investigated by looking at the values of the Bond number through the calibration process.

To begin the investigation, the density value that should have been used for the shear cell simulations was found first. This was done by using the poured bulk density measurements for each powder sample. Since DEM particles are essentially modeling a collection of smaller real particles as shown previously in Figure 2.5, the poured bulk density was scaled up by the random packing solid fraction of spheres which is approximately equal to 0.6 (Finney, 1970; Scott and Kilgour, 1969). Now after calibration of μ_{pp} and γ_{pp} , the simulation particle size was reduced to half the original size while keeping all the dimensionless parameter values the same. But at this point previously in this work, the Bond number was not scaled since it was not a part of the original set of dimensionless parameters. Thus, to continue the investigation, the Bond number was scaled as well.

When the particle size was scaled, the γ_{pp} variable also had to be scaled down to half to maintain the calibrated value for $\frac{\gamma_{pp}}{E^*d}$. Thus, the scaling of the Bond number $\left(\frac{\rho g d^2}{\gamma_{pp}}\right)$ could only be done successfully by doubling the ρ parameter as g is a constant and changing the halved γ_{pp} will affect the values of the other dimensionless parameters. Hence, the particle density, ρ , was doubled while keeping the dimensionless parameter values constant. At this point, the density values that were used for the Flodex simulations were compared to the density value that should have been used for these simulations found using the Bond number scaling. These two density values were found to be close to each other in magnitude which explains the calibration success.

To give an example of the numerical analysis described above, the ABT-089 powder sample can be used. The poured bulk density of ABT-089 is 0.330 g/cm³, this value when scaled up by 0.6 is equal to 0.550 g/cm³. This 0.550 g/cm³ is the value that should have been used in the shear cell simulations. But a fixed particle density value of 1.0 g/cm³ was used instead. Now, the shear cell is not sensitive to this parameter and consequently, this value being different from the scaled-up value did not affect the shear cell results. But, if the right value for the particle density was used in the initial shear cell simulation, the Flodex particle density after scaling the Bond number should have been 1.1 g/cm³. This value is very close to the fixed value of density, 1.0 g/cm³, used for all the DEM simulations. Thus, the fixed value resulted in accurate modeling of the Flodex simulations even while not considering the density parameter values. This sensitivity of Flodex simulations to density can be further explored and the test could be used as a bulk calibration test for particle density.

7. SUMMARY AND CONCLUSIONS

The primary goal of this work was to develop a validated methodology to calibrate DEM parameters using dimensional analysis to increase generality. This methodology was developed using a DEM simulation of an annular shear cell. A single device with multiple possible bulk measurements was used for calibration to make it as simple as possible and robust in its practical application.

The experimental measurements for three powders were carried out using a Schulze ring shear cell tester RST-XS and a section of the shear cell was modeled in DEM with the use of EDEM using periodic boundaries while using the Hertzian contact model with simplified JKR cohesion. The input parameters required for the DEM simulation were isolated and a dimensional analysis was conducted on these parameters to find dimensionless parameters that can capture the bulk responses of the shear cell. The three bulk responses used were the incipient yield internal friction angle, critical state internal friction angle, and the bulk cohesion.

A factorial study was set up using a design of experiments and a set of simulations were set up using these preset dimensionless parameter values to select the DEM input parameter values. All insignificant parameters were eliminated prior to the setup of the factorial study to reduce the number of simulation sets to be run. The use of a factorial study enabled the study of interaction effects between parameters along with the main effects of each parameter on the bulk response. This is critical in mapping the complete parameter space instead of only the corners as typically only one parameter is changed at a time. Using MANOVA analysis on the results of these simulations, models were created for each of the three bulk responses. A constant term was added to each model to better accommodate the non-significant remaining parameter contributions. It was found that all the three bulk responses had either primary and/or secondary dependence on both the sliding friction and dimensionless cohesion parameter. The consolidation stress was also shown to be statistically significant but since it is an experimental parameter, the future calibration was done for each fixed value of the consolidation stress and its contribution was absorbed by the constant term in the models.

The models created using the shear cell had unknown coefficients which were then found using regression. At this stage, the predicted models created were ready to be calibrated against experimental measurements made using the shear cell on each powder at different end

consolidation stress values. Since there were only two parameters to be calibrated, only two bulk responses were used, the incipient internal friction angle and the bulk cohesion. The calibration was done using a multi-objective function optimization using residual error comparisons between the predictive model and the experimental measurements. A genetic algorithm was used to do the multi-objective optimization.

DEM parameter calibrations typically result in multiple parameter value solutions (Grima and Wypych, 2011; Ranjan, 2017). This issue was anticipated and thus when doing the multiple objective optimization using the genetic algorithm, a convergence parameter was utilized. Thus, to eliminate this issue, the convergence of both residual values for the objective functions was required and the best set of values was chosen. Ideally, two bulk calibration tests should be used to calibrate for the same parameter and the calibrated values that overlap should be used for the final validation. This eliminates the issue of multiple solutions while helping find the best optimal calibrated value for that specific parameter. This was done in the current work by using two bulk outputs each dependent on two parameters and calibrating by using the overlap where both the bulk outputs were modeled with the least error.

Additionally, it was found that the calibrated sliding friction value for different end consolidation stress values did not change significantly but the cohesion surface energy density value increased with an increase in the end consolidation stress value. Thus, a major limiting factor of this work is the interdependence of the calibrated cohesion parameter value with the end consolidation stress value. Ideally, the model should only have one value for a calibrated parameter for multiple stress values in a range. But due to the simplified nature of the cohesion model used, the stress dependence of cohesion forces was not incorporated in the model and led to this limitation. This restricts the applications of the model to experiments or simulations where stress states are known or do not vary considerably. A more involved cohesion model or a modification of the current model to incorporate the stress dependence would address this limitation. This could potentially require calibration of an additional parameter value and thus another bulk calibration experiment.

The calibration success was measured using the value of the residual at the calibrated value and partially validated using a simulation for the third bulk response, the critical state internal friction angle, at the calibrated values and comparing it to experimental measurement. It was

noticed that the HPMC calibration error and the partial validation errors were significantly high compared to Lactose and ABT-089.

This unusual difference was amounted to the HPMC powder particles being smaller and fibrous which would interlock during shear leading to different behavior compared to the simulations. This was addressed by changing the particle shape from spherical particles to a glued sphere particle with an aspect ratio of two made up of five overlapping spheres. This improved the accuracy significantly and progressed results within the chosen error convergence value of 5%. Thus, particle shape factor was concluded to be an important parameter in terms of DEM calibration especially for powder particles with more deviation from spherical particles.

To test the success of the calibration, the calibrated parameter values need to be tested on an independent test. A flow through an orifice test using a Flodex was used as the validation experiment. But since one of the two calibrated parameters is dependent on the stress on the particle, a regression model had to be created with the data points available. To find the stress on a particle in the Flodex, hydrostatic pressure calculation at the bottom particle layer was used and the calibrated value was found using interpolation between the known values.

The Flodex device has a standard deviation of ± 1 mm for the measurements. The validation using the Flodex showed that the model slightly overpredicted the Flowability index by 2 mm for Lactose while accurately predicting the results for ABT-089 with simulations with spherical particles. For HPMC, the simulations with non-spherical particles with an aspect ratio of two slightly underpredicted by the Flowability index by 2 mm. All the differences were within one disk diameter change (2 mm) in the Flodex. Further, a factory size and height sensitivity analysis was done for the Flodex test. This analysis showed no significant sensitivity to the factory size and diameter. For Lactose, the overprediction increased by another disk diameter change. This change was amounted to large mound formations due to the substantially high ratio of DEM particle diameter to the factory height compared to real particle diameter and factory height.

This work highlighted the importance of dimensional analysis by illustrating the ease at which the parameter values can be changed while maintaining the dimensionless parameter values. It can be concluded that an annular shear cell is a great device for bulk calibration. It has two different outputs, incipient internal friction angle and bulk cohesion, that can be used to calibrate two different parameters with one measurement. It also highlighted how adaptable the parameter value changes are while not affecting the simulation results as long as dimensionless parameter

values are kept constant. This can be used extensively to simplify simulations and radically improve simulation times. While there are multiple ways the calibration success of DEM parameters can be improved, this work highlights that simpler methodologies are efficient in the calibration of DEM parameters and predicting real world powder behavior. Furthermore, these simpler methodologies can be used as a starting point in extensive calibration studies by eliminating parameters prior to the massive computational costs associated with larger studies.

8. RECOMMENDATION FOR FUTURE WORK

The current work utilized an annular shear cell bulk response and calibrated DEM parameters using it. This calibrated model effectively predicted flow behavior by replicating the results of an independent validation experiment using a DEM simulation. Although the models made using DEM presented in this work predicted flow behavior accurately, there are still improvements to be made. Based on the experience gained through the procedure, and the observations made, several future recommendations can be made.

The calibration was performed for the particle-particle sliding friction (μ_{pp}) and particle-particle cohesive surface energy density (γ_{pp}) parameters. Additionally, the current work utilized an annular shear cell with fins to eliminate any significant particle-geometry interactions. Since the particle-geometry interaction parameters were not investigated, they should be explored next. Particle-geometry interactions are critical to predicting flow behavior in various processes involving extensive particle-geometry contact. The calibration methodology can be repeated utilizing the current calibrated particle-particle parameters and utilizing a shear cell with no fins along with a material slab of the geometry being investigated to accurately look at particle-geometry interactions.

Since the statistically significant parameters were found to be the sliding friction parameter and the cohesive surface energy parameter, it is important to explore these two parameters further. A suggestion would be to extend the parameter values to see how the dependence changes at more extreme values for both parameters and which parameter takes precedence. The bulk responses sensitive to the two parameters could potentially increase exponentially in their sensitivity at higher value ranges.

In addition, the cohesion model used in this work is a simplified JKR model with cohesion parameter only, the particle-particle cohesive surface energy density (γ_{pp}). This limits the extent to which the model can predict the cohesive behavior of the material while decreasing calibration time significantly. To address this limitation, the recommendation would be to extend the study with a better cohesion model with more parameters than the simplified JKR model to better capture the cohesive behavior while continuing to use the methodology laid out in the current work. This might also address the issue with the interdependence between the stress on the particle bed and

the cohesion surface energy density. If not, a more robust cohesion model can be created to incorporate this dependence within the model.

A recommendation for a more involved cohesion model would be using an Edinburg Elasto-Plastic Adhesion (EEPA) model as implemented in EDEM (Morrissey et al., 2014). This model is an extension of the linear hysteretic model by Walton and Braun, 1986. The six input parameters for this model would increase the computational work and time needed for the calibration effort considerably. This is because each of the six parameters would need to be calibrated depending on the sensitivity of the bulk output to each of them. This model can be implemented and calibrated using the approach laid out in the current work. Although the name includes adhesion between dissimilar materials, the model can be used for cohesion between similar materials as well. Material subjected to high consolidation can experience plastic deformation which can affect the cohesive behavior because of the change in the surface contact area. This model addresses this specific issue by simulating this behavior.

The force models used in DEM simulations also need to be explored. The model used in this thesis is a Hertzian contact model, but other models should be tested. A hysteretic spring model could be used to allow for plastic deformation behaviors to be added to the computation. It is a better representation of a compressible material since while using this model, large overlaps are possible without extreme forces acting on the particles like in the current model. The hysteretic spring model follows different curves for the loading and unloading of material. The force-displacement behavior for the same is as shown in Figure 8.1 below. In the EDEM implementation of the hysteretic spring model, the tangential force component is modeled identically to the tangential forces from a linear spring model.

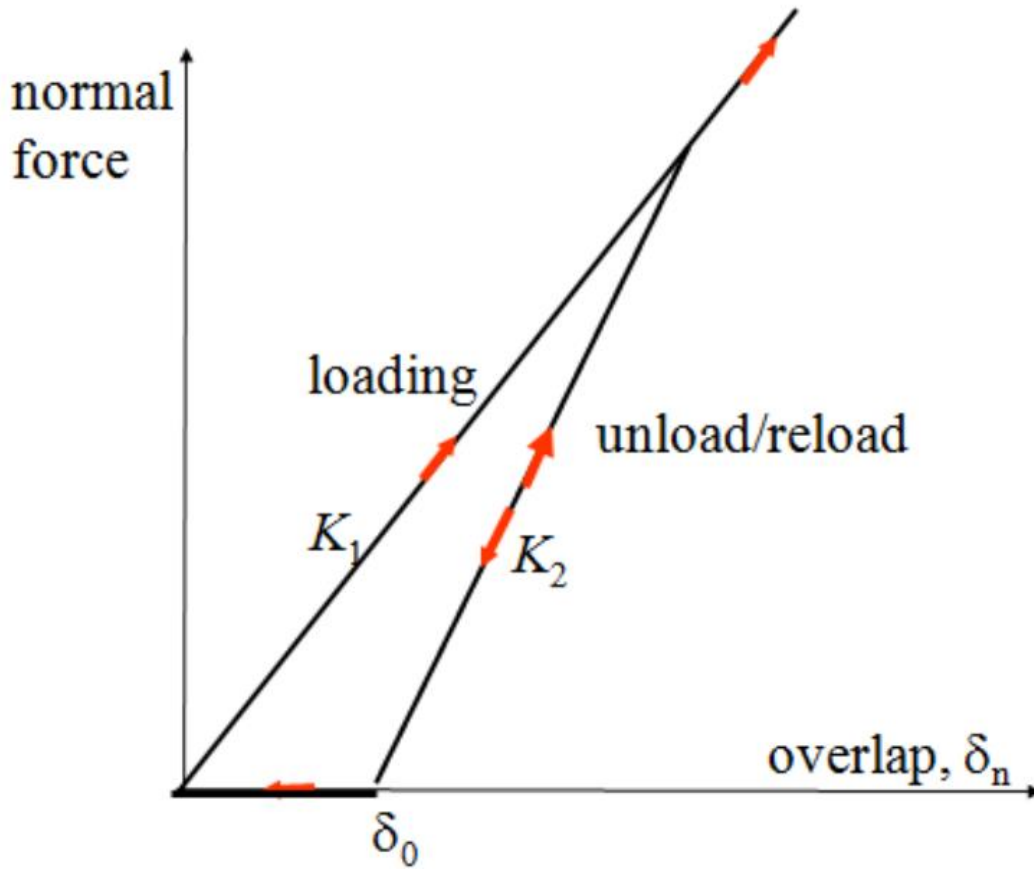


Figure 8.1: Schematic of the linear Hysteretic Spring contact model force-displacement relationship showing different loading and unloading curves with the red arrows showing the loading directions

The dimensionless particle size distribution parameter showed little to no statistical significance on all three of the output responses for the shear cell. This could be due to a restrictive small range of values chosen, a wider parameter value range could confirm that the particle size distribution does not significantly affect the bulk response output. The DEM particle sizes are larger than the particles being studied to reduce the simulation time. When DEM particle size is too close to the geometry being analyzed, there can be issues with particle packing and mechanical arching, leading to inaccurate process modeling. Thus, the particle size could be reduced further for more confirmation in the DEM results.

Another aspect of the particle size distribution to look at would be the type of distribution used. The current thesis work utilizes a normal Gaussian distribution, but other studies have

successfully used log-normal distributions to also predict cohesive powder flow behavior accurately. Thus, to conclude, the recommendation for the particle size distribution parameter would be to widen the range of values used, try decreased particle diameter size, and to model it using a different type of distribution.

For the HPMC calibration, the particle shape factor in the form of an aspect ratio was added to improve calibration results. It significantly increased the calibration accuracy for the HPMC powder sample. Including a particle shape factor like an aspect ratio and developing a non-spherical particle geometry to use in these bulk calibration simulations would improve the calibration robustness and improve the characterization of different material behavior. This aspect ratio parameter could be incorporated directly as an addition to the design of experiments parameters in the factorial study. It can be an additional parameter to calibrate for after checking the sensitivity of the bulk response to the parameter.

The flow through an orifice is a good indicator of powder flowability. The Flodex operating procedure as given by Hanson Research utilizes this principle in their three successful passes approach. This is adequate but utilizing a more robust approach is recommended. A recommended approach would be to run 10 tests for each orifice diameter and check for failure or success for each pass. The result would be a percentage indicator for each orifice diameter. This approach is more reliable and repeatable compared to the three consecutive passes method. It gives a better representation of the powder flowability as well and facilitates the comparison of powder flowability between samples using the percent success curves. The downside being the time required to run the simulations and perform the experimental measurements as this method involves a substantially larger number of simulations. To minimize the number of simulations, a preliminary check with one run each can be done at each orifice diameter and only investigate the orifice sizes in the vicinity of the flow and no-flow region.

REFERENCES

- Alizadeh, Ebrahim, François Bertrand, and Jamal Chaouki. 2014. “Discrete Element Simulation of Particle Mixing and Segregation in a Tetrapodal Blender.” *Computers & Chemical Engineering* 64: 1–12.
- Allenspach, Carl. 2020. “Directly Compressible Hydroxypropyl Methylcellulose (HPMC) to Support Continuous Manufacturing.”
- Allenspach, Carl, Peter Timmins, Shasad Sharif, and Tamara Minko. 2020. “Characterization of a Novel Hydroxypropyl Methylcellulose (HPMC) Direct Compression Grade Excipient for Pharmaceutical Tablets.” *International Journal of Pharmaceutics* 583: 119343.
<https://www.sciencedirect.com/science/article/pii/S0378517320303276>.
- Anand, Anshu et al. 2008. “Predicting Discharge Dynamics from a Rectangular Hopper Using the Discrete Element Method (DEM).” *Chemical Engineering Science* 63(24): 5821–30.
- Angus, Andrew et al. 2020. “Calibrating Friction Coefficients in Discrete Element Method Simulations with Shear-Cell Experiments.” *Powder Technology* 372: 290–304.
- Asaf, Z, D Rubinstein, and I Shmulevich. 2007. “Determination of Discrete Element Model Parameters Required for Soil Tillage.” *Soil and Tillage Research* 92(1): 227–42.
<https://www.sciencedirect.com/science/article/pii/S0167198706000638>.
- Behjani, Mohammadreza Alizadeh, Nejat Rahmanian, and Ali Hassanpour. 2017. “An Investigation on Process of Seeded Granulation in a Continuous Drum Granulator Using DEM.” *Advanced Powder Technology* 28(10): 2456–64.
- Benvenuti, L, C Kloss, and S Pirker. 2016. “Identification of DEM Simulation Parameters by Artificial Neural Networks and Bulk Experiments.” *Powder technology* 291: 456–65.
- Bolton, M D. 1986. “The Strength and Dilatancy of Sands.” *Geotechnique* 36(1): 65–78.
- Bray, James H, Scott E Maxwell, and Scott E Maxwell. 1985. *Multivariate Analysis of Variance*. Sage.
- Chen, Xizhong, and James A Elliott. 2020. “On the Scaling Law of JKR Contact Model for Coarse-Grained Cohesive Particles.” *Chemical Engineering Science* 227: 115906.
<https://www.sciencedirect.com/science/article/pii/S0009250920304383>.
- Chen, Ying, Lars J Munkholm, and Tavs Nyord. 2013. “A Discrete Element Model for Soil–Sweep Interaction in Three Different Soils.” *Soil and Tillage Research* 126: 34–41.

- Coetzee, C J. 2017. “Calibration of the Discrete Element Method.” *Powder Technology* 310: 104–42.
- Cundall, Peter A, and Otto D L Strack. 1979. “A Discrete Numerical Model for Granular Assemblies.” *geotechnique* 29(1): 47–65.
- DEM Solutions. 2014. *EDEM Theory Reference Guide*.
https://www.edemsimulation.com/content/uploads/2016/08/EDEM2.6_theory_reference_guide.pdf.
- Favier, J F, M H Abbaspour-Fard, M Kremmer, and A O Raji. 1999. “Shape Representation of Axi-symmetrical, Non-spherical Particles in Discrete Element Simulation Using Multi-element Model Particles.” *Engineering computations*.
- Finney, J L. 1970. “Random Packings and the Structure of Simple Liquids. I. The Geometry of Random Close Packing.” *Proceedings of the Royal Society of London. A. Mathematical and Physical Sciences* 319(1539): 479–93.
- Gallas, Jason A C, and Stefan Sokolowski. 1993. “Grain Non-Sphericity Effects on the Angle of Repose of Granular Material.” *International Journal of Modern Physics B* 7(09n10): 2037–46.
- Geiger, Derek, Mark Wandstrat, and Paul Mort. 2007. “Granular Flow through an Orifice—Effect of Granule Properties on the Onset of Jamming.” In AICHE Annual Meeting Salt Lake City, USA.
- Grima, Andrew Phillip, and Peter Wilhelm Wypych. 2011. “Development and Validation of Calibration Methods for Discrete Element Modeling.” *Granular Matter* 13(2): 127–32.
- Guo, Y et al. 2013. “Granular Shear Flows of Flat Disks and Elongated Rods without and with Friction.” *Physics of Fluids* 25(6): 63304.
- Guo, Yu, C-Y Wu, K D Kafui, and Colin Thornton. 2011. “3D DEM/CFD Analysis of Size-Induced Segregation during Die Filling.” *Powder Technology* 206(1–2): 177–88.
- Guo, Yuan et al. 2021. “A Nonlinear Elasto-Plastic Bond Model for the Discrete Element Modeling of Woody Biomass Particles.” *Powder Technology* 385: 557–71.
- Hærvig, J et al. 2017. “On the Adhesive JKR Contact and Rolling Models for Reduced Particle Stiffness Discrete Element Simulations.” *Powder Technology* 319: 472–82.
<https://www.sciencedirect.com/science/article/pii/S0032591017305430>.

- Hanley, Kevin J et al. 2011. "Application of Taguchi Methods to DEM Calibration of Bonded Agglomerates." *Powder technology* 210(3): 230–40.
- Hanson Research Corporation. 2004. *Flodex Operation Manual 21-101-000*. Chatsworth, CA.
- Hassanpour, A, and M Ghadiri. 2004. "Distinct Element Analysis and Experimental Evaluation of the Heckel Analysis of Bulk Powder Compression." *Powder Technology* 141(3): 251–61.
- Johnson, Kenneth Langstreth, Kevin Kendall, and aAD Roberts. 1971. "Surface Energy and the Contact of Elastic Solids." *Proceedings of the royal society of London. A. mathematical and physical sciences* 324(1558): 301–13.
- Kamrin, Ken. 2010. "Nonlinear Elasto-Plastic Model for Dense Granular Flow." *International Journal of Plasticity* 26(2): 167–88.
- Karkala, Subhodh et al. 2019. "Calibration of Discrete-Element-Method Parameters for Cohesive Materials Using Dynamic-Yield-Strength and Shear-Cell Experiments." *Processes* 7(5): 278.
- Ketterhagen, William R. 2018. "Discrete Element Method (DEM) Investigation of Particle Properties on Bulk Powder Flowability: Toward a Particle Calibration Library for Pharmaceutical Materials." In *8th World Congress on Particle Technology. AIChE, 2018*.
- Ketterhagen, William R., Jennifer S. Curtis, Carl R. Wassgren, and Bruno C. Hancock. 2009. "Predicting the Flow Mode from Hoppers Using the Discrete Element Method." *Powder Technology* 195(1): 1–10.
<https://www.sciencedirect.com/science/article/pii/S0032591009003088> (September 25, 2019).
- Ketterhagen, William R et al. 2007. "Granular Segregation in Discharging Cylindrical Hoppers: A Discrete Element and Experimental Study." *Chemical Engineering Science* 62(22): 6423–39.
- Kodam, Madhusudhan et al. 2009. "Force Model Considerations for Glued-Sphere Discrete Element Method Simulations." *Chemical Engineering Science* 64(15): 3466–75.
<https://www.sciencedirect.com/science/article/pii/S0009250909002747>.
- Kretz, D et al. 2016. "Discrete Element Method (DEM) Simulation and Validation of a Screw Feeder System." *Powder Technology* 287: 131–38.
<https://www.sciencedirect.com/science/article/pii/S0032591015300851>.

- Kumar, Vijay, Michael K Taylor, Amit Mehrotra, and William C Stagner. 2013. "Real-Time Particle Size Analysis Using Focused Beam Reflectance Measurement as a Process Analytical Technology Tool for a Continuous Granulation–Drying–Milling Process." *Aaps Pharmscitech* 14(2): 523–30.
- Lavoie, François, Louis Cartilier, and Roch Thibert. 2002. "New Methods Characterizing Avalanche Behavior to Determine Powder Flow." *Pharmaceutical research* 19(6): 887–93.
- Leisen, D, I Kerkamm, E Bohn, and M Kamlah. 2012. "A Novel and Simple Approach for Characterizing the Young's Modulus of Single Particles in a Soft Matrix by Nanoindentation." *Journal of Materials Research* 27(24): 3073–82.
- Loreti, Simone, and Chuan-Yu Wu. 2018. "Three-Dimensional Discrete Element Modeling of Three Point Bending Tests: The Effect of Surface Energy on the Tensile Strength." *Powder Technology* 337: 119–26.
<https://www.sciencedirect.com/science/article/pii/S0032591017309737>.
- Lu, MMGR, and G R McDowell. 2007. "The Importance of Modeling Ballast Particle Shape in the Discrete Element Method." *Granular matter* 9(1–2): 69.
- Marigo, M., D. L. Cairns, J. Bowen, and A. Ingram. 2014. "Relationship between Single and Bulk Mechanical Properties for Zeolite ZSM5 Spray-Dried Particles." *Particuology* 14: 130–38.
- Marigo, M et al. 2011. "Developing Mechanistic Understanding of Granular Behaviour in Complex Moving Geometry Using the Discrete Element Method: Part B: Investigation of Flow and Mixing in the Turbula® Mixer." *Powder technology* 212(1): 17–24.
- Martin, C L, and D Bouvard. 2003. "Study of the Cold Compaction of Composite Powders by the Discrete Element Method." *Acta Materialia* 51(2): 373–86.
- Mathews, Paul G. 2005. 446 *Design of Experiments with MINITAB*. ASQ Quality Press Milwaukee, WI, USA:
- Mindlin, R D, and H Deresiewicz. 1953. *Timoshenko's Shear Coefficient for Flexural Vibrations of Beams*. COLUMBIA UNIV NEW YORK.
- Morrissey, John P, Subhash C Thakur, and J Y Ooi. 2014. "EDEM Contact Model: Adhesive Elasto-Plastic Model." *Granul. Matter* 16(3): 383–400.
- Nolan, G T, and P E Kavanagh. 1995. "Random Packing of Nonspherical Particles." *Powder technology* 84(3): 199–205.

- Obermayr, Martin, Christos Vrettos, Peter Eberhard, and Thomas Däuwel. 2014. “A Discrete Element Model and Its Experimental Validation for the Prediction of Draft Forces in Cohesive Soil.” *Journal of Terramechanics* 53: 93–104.
- Owen, P J, and P W Cleary. 2009. “Prediction of Screw Conveyor Performance Using the Discrete Element Method (DEM).” *Powder Technology* 193(3): 274–88.
- Ranjan, Harsh. 2017. “A Methodology for DEM Parameter Calibration.”
- Di Renzo, Alberto, and Francesco Paolo Di Maio. 2004. “Comparison of Contact-Force Models for the Simulation of Collisions in DEM-Based Granular Flow Codes.” *Chemical Engineering Science* 59(3): 525–41.
- Ristow, Gerald H. 1994. “Granular Dynamics: A Review about Recent Molecular Dynamics Simulations of Granular Materials.” *Annual reviews of computational physics I*: 275–308.
- Sadek, Mohammad A, Ying Chen, and Jude Liu. 2011. “Simulating Shear Behavior of a Sandy Soil under Different Soil Conditions.” *Journal of Terramechanics* 48(6): 451–58.
- Schiano, Serena, Lan Chen, and Chuan-Yu Wu. 2018. “The Effect of Dry Granulation on Flow Behaviour of Pharmaceutical Powders during Die Filling.” *Powder Technology* 337: 78–83. <https://www.sciencedirect.com/science/article/pii/S0032591017307192>.
- Schulze, Dietmar. 2008. “Powders and Bulk Solids.” *Behaviour, characterization, storage and flow*. Springer 22.
- Schwedes, J, and D Schulze. 1990. “Measurement of Flow Properties of Bulk Solids.” *Powder Technology* 61(1): 59–68. <https://www.sciencedirect.com/science/article/pii/0032591090800668>.
- Scott, G D, and D M Kilgour. 1969. “The Density of Random Close Packing of Spheres.” *Journal of Physics D: Applied Physics* 2(6): 863.
- Shimizu, Yoshiyuki, and Peter A Cundall. 2001. “Three-Dimensional DEM Simulations of Bulk Handling by Screw Conveyors.” *Journal of engineering mechanics* 127(9): 864–72.
- Simons, Tom A H et al. 2015. “A Ring Shear Tester as Calibration Experiment for DEM Simulations in Agitated Mixers—a Sensitivity Study.” *Procedia engineering* 102: 741–48.
- Souihi, Nabil et al. 2013. “Design Space Estimation of the Roller Compaction Process.” *Industrial & Engineering Chemistry Research* 52(35): 12408–19.
- Tsuji, Yutaka, Toshihiro Kawaguchi, and Toshitsugu Tanaka. 1993. “Discrete Particle Simulation of Two-Dimensional Fluidized Bed.” *Powder technology* 77(1): 79–87.

- Ucgu, Mustafa, John M Fielke, and Chris Saunders. 2014. "Three-Dimensional Discrete Element Modeling of Tillage: Determination of a Suitable Contact Model and Parameters for a Cohesionless Soil." *Biosystems Engineering* 121: 105–17.
- United States Pharmacopeia and National Formulary. 2007. "USP 1174."
- Vu-Quoc, Loc, and Xiang Zhang. 1999. "An Accurate and Efficient Tangential Force–Displacement Model for Elastic Frictional Contact in Particle-Flow Simulations." *Mechanics of materials* 31(4): 235–69.
- Walton, Otis R, and Robert L Braun. 1986. "Viscosity, Granular-temperature, and Stress Calculations for Shearing Assemblies of Inelastic, Frictional Disks." *Journal of rheology* 30(5): 949–80.
- Weinfurt, Kevin P. 1995. "Multivariate Analysis of Variance."
- Wilkinson, S K et al. 2017. "A Parametric Evaluation of Powder Flowability Using a Freeman Rheometer through Statistical and Sensitivity Analysis: A Discrete Element Method (DEM) Study." *Computers & Chemical Engineering* 97: 161–74.
<https://www.sciencedirect.com/science/article/pii/S0098135416303817>.
- Williamson, David F, Robert A Parker, and Juliette S Kendrick. 1989. "The Box Plot: A Simple Visual Method to Interpret Data." *Annals of internal medicine* 110(11): 916–21.
- Wu, Chuan-Yu. 2008. "DEM Simulations of Die Filling during Pharmaceutical Tabletting." *Particuology* 6(6): 412–18.
- Yoon, Jeoungeok. 2007. "Application of Experimental Design and Optimization to PFC Model Calibration in Uniaxial Compression Simulation." *International Journal of Rock Mechanics and Mining Sciences* 44(6): 871–89.
- Zhang, Jiayuan et al. 2004. "Application of the Discrete Approach to the Simulation of Size Segregation in Granular Chute Flow." *Industrial & engineering chemistry research* 43(18): 5521–28.
- Zhang, Rui, and Jianqiao Li. 2006. "Simulation on Mechanical Behavior of Cohesive Soil by Distinct Element Method." *Journal of Terramechanics* 43(3): 303–16.
- Zhou, Y C, Bao Hua Xu, Ai-Bing Yu, and P Zulli. 2002. "An Experimental and Numerical Study of the Angle of Repose of Coarse Spheres." *Powder technology* 125(1): 45–54.